

RESEARCH ARTICLE

Diverse mechanisms regulate contractile ring assembly for cytokinesis in the two-cell *Caenorhabditis elegans* embryo

Imge Ozugergin, Karina Mastronardi*, Chris Law* and Alisa Piekny†

ABSTRACT

Cytokinesis occurs at the end of mitosis as a result of the ingression of a contractile ring that cleaves the daughter cells. The core machinery regulating this crucial process is conserved among metazoans. Multiple pathways control ring assembly, but their contribution in different cell types is not known. We found that in the *Caenorhabditis elegans* embryo, AB and P₁ cells fated to be somatic tissue and germline, respectively, have different cytokinesis kinetics supported by distinct myosin levels and organization. Through perturbation of RhoA or polarity regulators and the generation of tetraploid strains, we found that ring assembly is controlled by multiple fate-dependent factors that include myosin levels, and mechanisms that respond to cell size. Active Ran coordinates ring position with the segregating chromatids in HeLa cells by forming an inverse gradient with importins that control the cortical recruitment of anillin. We found that the Ran pathway regulates anillin in AB cells but functions differently in P₁ cells. We propose that ring assembly delays in P₁ cells caused by low myosin and Ran signaling coordinate the timing of ring closure with their somatic neighbors.

This article has an associated First Person interview with the first author of the paper.

KEY WORDS: Cytokinesis, RhoA GTPase, Myosin, Contractility, Ran GTPase

INTRODUCTION

We have extensive knowledge of the core cytokinesis machinery, but the mechanisms that regulate this machinery are less well understood. Cytokinesis occurs during mitotic exit because of the ingression of a RhoA-dependent contractile ring that assembles in the equatorial plane. The Rho guanine-nucleotide-exchange factor (GEF) Ect2 generates active RhoA in the equatorial plane, which directs the assembly of a contractile ring by recruiting effectors for F-actin polymerization and myosin activation. Consistent with its essential role in this process, Ect2 depletion causes cytokinesis failure in multiple cell types (Piekny et al., 2005; Green et al., 2012; Basant and Glotzer, 2018). In early anaphase, actomyosin filaments assemble as a broad equatorial band, and then transition into a tight ring that pinches in the overlying cortex (Lewellyn et al., 2010; Green et al., 2012; van Oostende Triplet et al., 2014). Various proteins control

ring closure kinetics via crosslinking actin or regulating myosin activity. The highly conserved protein anillin is a key regulator of cytokinesis that anchors the contractile ring to the membrane (Piekny and Maddox, 2010; Tse et al., 2011; van Oostende Triplet et al., 2014). In support of this function, anillin depletion causes ring oscillation and cytokinesis failure, or alters the symmetry of ring closure depending on the cell type (e.g. Maddox et al., 2007; Hickson and O'Farrell, 2008; Piekny and Glotzer, 2008).

Numerous spindle-dependent or -independent mechanisms regulate ring assembly. The prevailing dogma in the field is that the anaphase spindle determines the division plane through the spatiotemporal control of Ect2 (Piekny et al., 2005; Green et al., 2012; Basant and Glotzer, 2018). Ect2 activation requires binding to Cyk4 (also known as RACGAP1 and MgcRacGAP), which is part of the centralspindlin complex that builds the central spindle (Mishima et al., 2002; Somers and Saint, 2003; Yuce et al., 2005). The astral microtubules also restrict the localization of active RhoA to the equatorial plane, although the mechanisms regulating this are less clear (Dechant and Glotzer, 2003; Lewellyn et al., 2010; Tse et al., 2011; van Oostende Triplet et al., 2014). Signals from other locations of the cell, including kinetochores and chromatin, have also been shown to regulate cytokinesis (Kiyomitsu and Cheeseman, 2013; Zanin et al., 2013; Rodrigues et al., 2015; Beaudet et al., 2017; Mangal et al., 2018; Beaudet et al., 2020). However, their conservation and relative contribution in different cell types is not well defined, as few studies have been performed in comparable cell types (e.g. cells with different fates in the same organism; Davies et al., 2018; Husser et al., 2021). Spindle-independent pathways might be redundant in symmetrically dividing cells, but could be essential in cells that divide asymmetrically, or that have different ploidy or fate.

Cues associated with chromatin coordinate contractile ring position with segregating chromosomes in HeLa cells, but it is not known if this mechanism functions in other organisms and cell types *in vivo* (Kiyomitsu and Cheeseman, 2013; Beaudet et al., 2017, 2020; Ozugergin and Piekny, 2021). The GTPase Ran is activated by RCC1 (RanGEF) near chromatin and is inactivated by cytosolic RanGAP. Following nuclear envelope breakdown, a gradient of Ran-GTP forms with high levels near chromatin, and low levels near the cortex (Kalab et al., 2002, 2006; Clarke and Zhang, 2008). Importins can bind to spindle assembly factors with nuclear localization signals (NLSs), which generally impedes their function. The release of importins by Ran-GTP in the vicinity of chromatin permits these factors to become active (e.g. Gruss et al., 2001; Nachury et al., 2001; Wiese et al., 2001; Silljé et al., 2006). However, importin regulation is not 'one size fits all' and the binding of importins could also have positive effects on protein function. Specifically, importin binding is required for anillin function by facilitating its cortical localization and function for cytokinesis (Kiyomitsu and Cheeseman, 2013; Beaudet et al., 2017, 2020). In addition, membrane-localized importin- α and - β have

Department of Biology, Concordia University, Montreal, H4B 1R6, Canada.

*These authors contributed equally to this work

†Author for correspondence (alisa.piekny@concordia.ca)

DOI: 10.1242/jcs.258921; I.O., 0000-0001-8667-4943; K.M., 0000-0001-9860-8409; C.L., 0000-0002-6946-8029; A.P., 0000-0002-4264-6980

Handling Editor: David Glover

Received 17 May 2021; Accepted 29 December 2021

been observed by several groups (Beaudet et al., 2017; Brownlee and Heald, 2019). Therefore, we propose that the Ran gradient is an elegant system that can function across the cell, with opposing roles depending on the NLS protein (reviewed in Ozugergin and Piekny, 2021). Our hypothesis is that cortical NLS proteins are regulated by importin binding to ensure that the ring is positioned between the segregating chromosomes to avoid aneuploidy. However, the Ran-dependent regulation of cytokinesis has not been studied in other cell types, particularly *in vivo* where the requirement for this mechanism could vary with parameters such as size and fate.

Cytokinesis has been well characterized in the *Caenorhabditis elegans* P₀ zygote, which is influenced by anterior–posterior polarity. This cell divides asymmetrically to give rise to a larger, anterior AB cell whose descendants form multiple tissues, and a smaller, posterior P₁ cell fated to become the germline (Rose and Gonczy, 2014). Anterior–posterior polarity is controlled by the mutually exclusive distribution of anterior (PAR-3–PAR-6–PKC-3) and posterior (PAR-2–PAR-1) complexes along the cortex. The establishment of polarity depends on the asymmetric enrichment of actomyosin contractility, which occurs in response to sperm entry (Cowan and Hyman, 2007; Hoege and Hyman, 2013; Rose and Gonczy, 2014; Gan and Motegi, 2020). Polarity is maintained via feedback between the PAR proteins and the actomyosin system at the anterior cortex, although its control switches from regulation by RhoA to Cdc42 (Cowan and Hyman, 2007; Hoege and Hyman, 2013; Rose and Gonczy, 2014; Gan and Motegi, 2020). As the P₀ zygote enters anaphase, actomyosin appears as patches or clusters at the anterior and equatorial cortex (Munro et al., 2004; Tse et al., 2012). Compression-driven flows toward the equatorial cortex may help actomyosin filaments to accumulate and align correctly (Khaliullin et al., 2018).

Three temporal phases of cytokinesis have been defined based on visible cell shape changes: ring assembly, furrow initiation, and ring constriction (e.g. Lewellyn et al., 2010; Price and Rose, 2017; Khaliullin et al., 2018; Chan et al., 2019; Osorio et al., 2019). Multiple factors are likely to influence these phases, although not many studies have explored this. There is a negative correlation between the rate of ring constriction and cell size, which was proposed to help coordinate the timing of cytokinesis among differently sized cells during embryogenesis (Carvalho et al., 2009). Another study showed that cell fate underlies differences in cytokinesis at the four-cell stage, where unique kinetics were observed as a result of different extrinsic and intrinsic pathways that regulate formin-derived F-actin (Davies et al., 2018). However, neither study explored cytokinesis in AB versus P₁ cells, and the mechanisms governing ring assembly in these cell types remain poorly understood.

In this study, we show that AB and P₁ cells have distinct cytokinesis kinetics that are regulated by a combination of myosin levels and different Ran pathway components. We found that although AB cells have a rapid ring assembly phase, it is slower in P₁ cells where myosin levels are lower and more poorly organized, and assembly negatively correlates with cell size. Based on observations with partial NMY-2 or ECT-2 depletion, we found that slower ring assembly in P₁ cells is not strictly a result of myosin levels. Indeed, disrupting cell fate via depletion of PAR-1 or PAR-3 equalized kinetics. Further, increasing myosin levels were able to override the delay in tetraploid P₁ cells, which retained the ability to control ring assembly in response to size. Next, we found that the Ran pathway governs the differences in the ring assembly phase between AB and P₁ cells, but functions through different components in the two cell types. Our data suggest that the Ran

pathway regulates the anillin-like protein ANI-1 for cytokinesis in AB cells similar to HeLa cells, whereas it functions differently in P₁ cells. Having distinct mechanisms that delay ring assembly in germline precursor cells could be important for coordinating ring closure with their somatic neighbors for cell positioning during embryogenesis.

RESULTS

Cytokinesis occurs differently in AB and P₁ cells

Cytokinesis is likely to be differently regulated depending on the cell type. In particular, the mechanisms regulating contractile ring assembly likely vary with parameters including cell fate, ploidy and/or size. We studied cytokinesis of AB and P₁ cells in the early *C. elegans* embryo, which have different fates and sizes. Since cytokinesis has not been studied extensively in these cells before, we first characterized the different phases of cytokinesis. To do this, we imaged embryos co-expressing GFP::PLCδ^{PH} or mNeonGreen::PLCδ^{PH} (hereafter referred to as GFP::PH and mNeonGreen::PH, respectively) and mCherry::HIS-58 to visualize the membrane and chromatin, respectively, from anaphase onset until furrow closure with high temporal resolution (Fig. 1A; Fig. S1A). Kymographs produced from the images were used to measure the change in cell diameter until the end of ingression (Fig. S2A). Cytokinesis was not linear in AB or P₁ cells (Fig. 1B), and the inflection points of each averaged ingression curve were calculated to mathematically delineate three distinct temporal phases (Fig. 1C). The phases, which were previously defined, include (1) ring assembly as the time from anaphase onset until shallow indentation of the equatorial cortex, (2) furrow initiation as the time from shallow indentation until the membrane appears to be back-to-back, and (3) ring constriction as closure of the membrane (Osorio et al., 2019). We imaged GFP::NMY-2 to further support that the membrane can report for the different phases based on myosin localization (Fig. S2B; Green et al., 2012; Osorio et al., 2019). We also tested for variation between AB and P₁ cells in different ('unpaired') versus the same ('paired') embryos, by repeating our analysis using only sister pairs (Fig. S2C). We found that the average ingression curves generated from only paired cells were not considerably different from the dataset ('Control') that included both unpaired and paired cells. Paired AB cells showed a greater difference during the constriction phase, which might indicate that these cells inherently show more variability.

Our results showed that AB cells had shorter ring assembly compared to P₁ cells, while the ring constriction phase took longer (Fig. 1B,C). To determine whether the difference in ring assembly kinetics is related to the levels of cortical myosin or actin, we imaged AB and P₁ cells expressing GFP::NMY-2 or LifeAct::mKate2. We measured myosin or actin levels along the midplane cortex at furrow initiation, where the membrane is visibly pulled in and forms a 'V' (Fig. 1D, left). This is when actomyosin filaments would have 'maximally' assembled and begun to generate force. Myosin and actin localized with a bell-like distribution in AB cells, with higher peak levels in the furrow region compared to P₁ cells (Fig. 1D; Fig. S3A; Pimpale et al., 2020). In P₁ cells, myosin and actin levels were higher along the anterior cortex compared to the posterior (Fig. 1D; Fig. S3A). Thus, myosin and actin levels are unique to each cell type. Repeating this analysis with only sister pairs showed that there was no significant difference compared to our measurements from different embryos (Fig. S3B).

To determine if the differences in myosin levels contribute to the differences in cytokinesis between AB and P₁ cells, we partially depleted NMY-2 (Fig. S3C). Delays in ring closure were observed

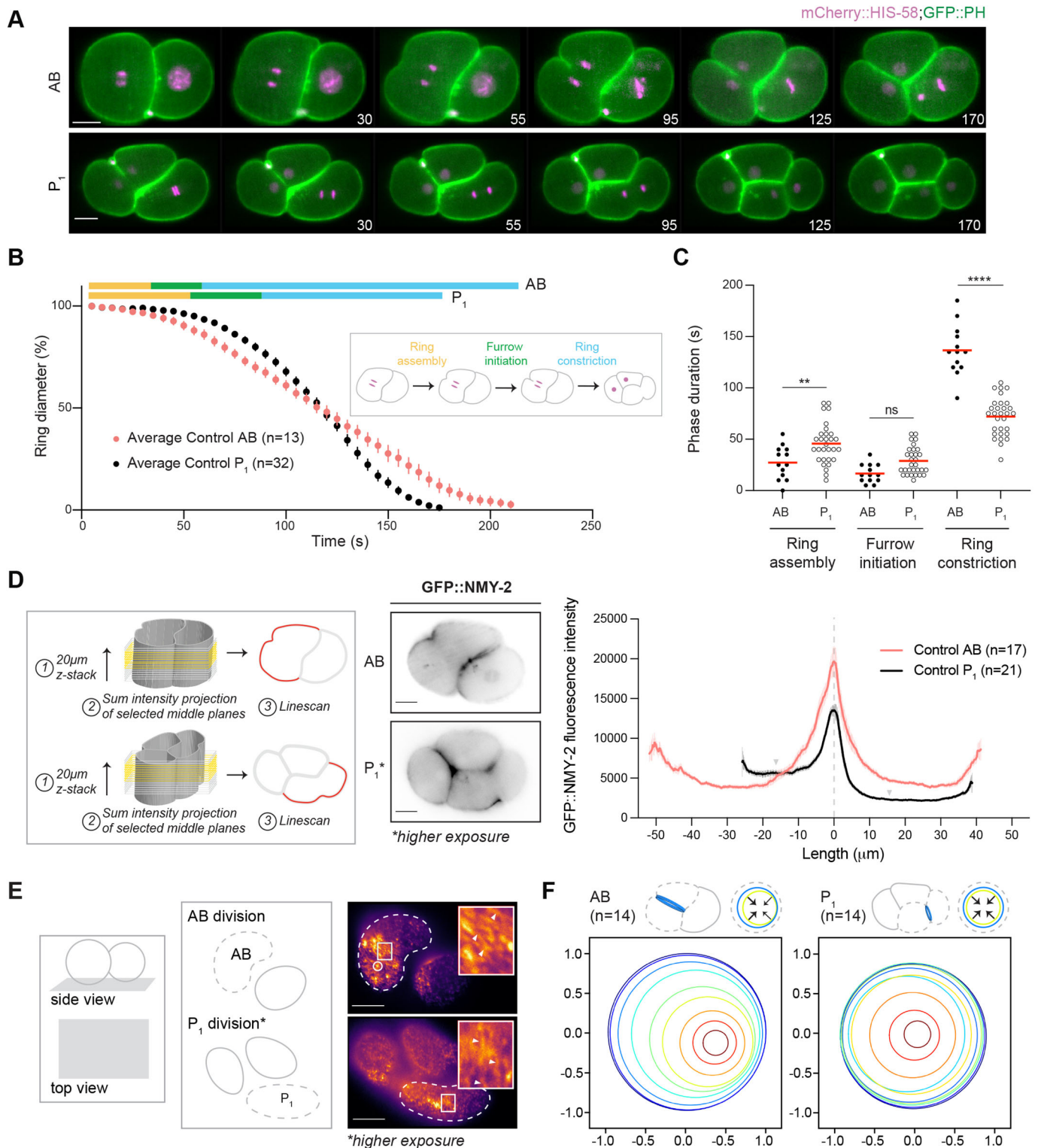


Fig. 1. AB and P₁ cells have unique cytokinesis kinetics. (A) Timelapse images show furrow ingression in AB and P₁ cells in embryos expressing mCherry::HIS-58 (magenta) and GFP::PH (green). (B) Cartoon schematics and a graph show the phases of ring closure in AB and P₁ cells. Bars show the duration of ring assembly, furrow initiation and ring constriction. (C) A plot shows ring closure phases in individual cells (mean, red lines; ** $P \leq 0.01$; **** $P \leq 0.0001$; ns, not significant; two-way ANOVA). (D) Left: schematics show how GFP::NMY-2 levels were measured at the midplane cortex. Middle: inverted images show myosin localization in AB and P₁ cells at furrow initiation. Right: graph showing GFP::NMY-2 accumulation in AB and P₁ cells [furrow, dashed gray line; gray arrowheads indicate anterior (left) and posterior (right) cortex]. (E) Left and middle: cartoon schematics show the planes visualized by HILo imaging (cells outlined by dashed lines). Right: Pseudocolored HILo images show GFP::NMY-2 in AB (top) and P₁ (bottom) cells. The circle outlines a myosin cluster. Arrowheads in the zoomed images (boxes) point to myosin filament bundles. (F) Cartoons show end-on ring closure. Ring closure is shown over time, with each timepoint as a different color. X- and y-axes indicate ratios of the distance from the starting position (0). Scale bars: 10 μ m. Data in B and D are expressed as mean \pm s.e.m.

in both cell types after partial RNAi as expected, but the relative differences in their kinetics was not altered (Fig. S3C). For example, the ring assembly phase still took longer relative to constriction in P₁ compared to AB cells. This suggests that differences in cytokinesis kinetics are not simply caused by myosin levels.

We also compared how myosin filament bundles are organized, as this could influence ring kinetics. We used highly inclined and laminated optical sheet (HILO) microscopy to visualize GFP::NMY-2 at the cortex in AB and P₁ cells (Fig. 1E). As reported previously, we observed an asymmetric, rotational wave of myosin in AB cells (Fig. 1E; Movie 1; Singh and Pohl, 2014). We also saw clusters of myosin flowing towards the equatorial zone, resembling those seen during pseudocleavage (Munro et al., 2004; Tse et al., 2012). In contrast, there were no clusters or cortical flow in P₁ cells (Fig. 1E; Movie 2), as observed by Pimpale et al. (2020).

Next, we measured the symmetry of ring closure. To measure symmetry, we compared the position of the ring before ingression to where it closes. Rings that closed in the middle were considered to be symmetric (<0.2) compared to those that closed near the periphery (>0.2; Fig. S3D). As reported by Bai et al. (2020), we found that ring closure was more asymmetric in AB versus P₁ cells, where ingression occurred toward the AB–P₁ cell boundary (Fig. 1F; Fig. S3D). To determine whether dividing AB cells can affect the symmetry of ring closure in P₁ cells, we also separately analyzed ‘influenced’ P₁ cells, where the division plane shifted because of the dividing AB cell. We did not observe any differences in symmetry for influenced compared to influence-free P₁ cells (Fig. S4A).

Contractility controls the rate of ring assembly

Although the relative differences in cytokinesis kinetics was maintained in AB and P₁ cells after partial depletion of NMY-2, upstream regulators of actomyosin could contribute to different kinetics by controlling F-actin levels or actomyosin organization. Active RhoA is required for actin polymerization and myosin bipolar filament assembly, and is regulated by the GEF ECT-2 (Fig. 2A; Green et al., 2012). We partially depleted ECT-2 to avoid phenotypes in the germline or P₀ zygote, and only considered embryos at the threshold required to support furrowing in AB and P₁ cells. Cytokinesis kinetics were strikingly similar to the partially depleted NMY-2 embryos, where ring closure was delayed, but relative differences were retained between AB and P₁ cells (Fig. 2B,C; Fig. S1B). This finding suggests that ECT-2-independent factors control the ring assembly phase differently in AB versus P₁ cells.

To correlate changes in myosin localization with cytokinesis phenotypes, we measured myosin levels along the midplane of *ect-2(RNAi)* embryos. There were narrower peaks of myosin in both AB and P₁ cells compared to their control counterparts, and it was no longer asymmetrically distributed in P₁ cells (Fig. 2D). The average peak value of myosin in AB cells was 68% of control levels, but similar between control and *ect-2(RNAi)* P₁ cells (Fig. 2E). Additionally, we measured total accumulated myosin levels in the furrow region by calculating the area under the peak (Fig. 2F). The total accumulated myosin levels in *ect-2(RNAi)* AB and P₁ cells were 57% and 58% compared to their control counterparts, and total levels in *ect-2(RNAi)* AB cells dropped to those in control P₁ cells (Fig. 2F). These data suggest that the levels of myosin in the furrow region are well above the threshold needed to support cytokinesis in AB cells, whereas P₁ cells operate closer to this threshold. To validate this, we repeated our analysis in *ect-2(RNAi)* embryos where cells formed a furrow, but ultimately failed cytokinesis (Fig. 2G; Fig. S5A, Movie 3). Indeed, myosin levels in AB cells that failed cytokinesis

were similar to P₁ cells that succeeded, whereas the levels in P₁ cells that failed cytokinesis dropped even lower (Fig. 2G).

To assess how ECT-2 depletion changes myosin organization, we performed HILO imaging of myosin in *ect-2(RNAi)* AB and P₁ cells (Fig. 2H; Movie 4). There was a dramatic loss in clusters and decreased rotational flow in AB cells compared to control cells (Fig. 2H; Pimpale et al., 2020). We also observed that myosin had a more punctate pattern with fewer filament bundles compared to control cells (Fig. 2H). Since flows are predicted to align myosin filaments in the ring, we determined the frequency of filament bundles in a defined region of the furrow where 0° reflects full alignment and considered the proportion within two standard deviations of the central peak (Fig. S5B). Although there was a high frequency of aligned filament bundles in both control AB and P₁ cells, there was a higher proportion within two standard deviations in AB cells compared to P₁ cells (‘amount’; Fig. S5B). In *ect-2(RNAi)* AB and P₁ cells, we observed an increase in the frequency of filament bundles with angles that deviate from 0°, and a decrease in the amount of aligned filaments (compare Fig. 2H and Fig. S5C with Fig. 1E and Fig. S5B). We observed even poorer filament organization in *ect-2(RNAi)* AB and P₁ cells that failed cytokinesis (Fig. S5D,E). Thus, the poor alignment of filament bundles in *ect-2(RNAi)* AB cells could reflect a loss of cortical flows, and the loss of alignment in both cells would support the delayed kinetics. Despite a change in kinetics, we found that ring closure remained symmetric in *ect-2(RNAi)* P₁ cells, and asymmetric in AB cells (Fig. 2I; Figs S3D and S4B).

Cell fate determines the rate of ring assembly

Our findings suggest that several parameters contribute to ring assembly that extend beyond actomyosin levels. To determine whether these parameters are fate dependent, we assessed cytokinesis in *par-1(RNAi)* and *par-3(RNAi)* embryos. As described earlier, the P₀ zygote divides asymmetrically to give rise to AB and P₁ cells, which is controlled by anterior and posterior complexes containing PAR-3 and PAR-1, respectively (Cowan and Hyman, 2007; Hoege and Hyman, 2013; Rose and Gonczy, 2014; Gan and Motegi, 2020). The loss of either PAR complex should equalize cell fate, but depletion of posterior PAR-1 should cause higher cortical contractility and AB-like kinetics, whereas the loss of anterior PAR-3 should cause lower contractility and P₁-like kinetics (Munro et al., 2004; Cowan and Hyman, 2007). *Par-3(RNAi)* and *par-1(RNAi)* P₀ daughter cells were equal in size and divided synchronously (Fig. 3A; Fig. S1C; Kemphues et al., 1988). However, *par-3(RNAi)* and *par-1(RNAi)* cells had kinetics that were similar to AB cells (Fig. 3B,C).

Next, we determined whether myosin levels and/or the organization of myosin filaments support the rapid kinetics in the PAR-depleted cells. Indeed, peak myosin levels were between those of control AB and P₁ cells [90% versus AB for *par-1(RNAi)* and 86% versus AB for *par-3(RNAi)*], and total accumulated levels in PAR-depleted cells were comparable to control AB cells (Figs 2E,F and 3D,F). Furthermore, HILO imaging revealed strong cortical flows and broad swaths of densely packed filament bundles that appeared to be well-aligned in the furrow region of *par-1(RNAi)* cells (Fig. 3E; Movie 5). Strong cortical flows could facilitate the localization and alignment of myosin filament bundles to support their enhanced kinetics. Interestingly, ring closure occurred asymmetrically in *par-3(RNAi)* and *par-1(RNAi)* P₀ daughter cells, similar to AB cells (Fig. 3G; Figs S3D, S4C,D). These data show that the differences in actomyosin between AB and P₁ cells are fate dependent.

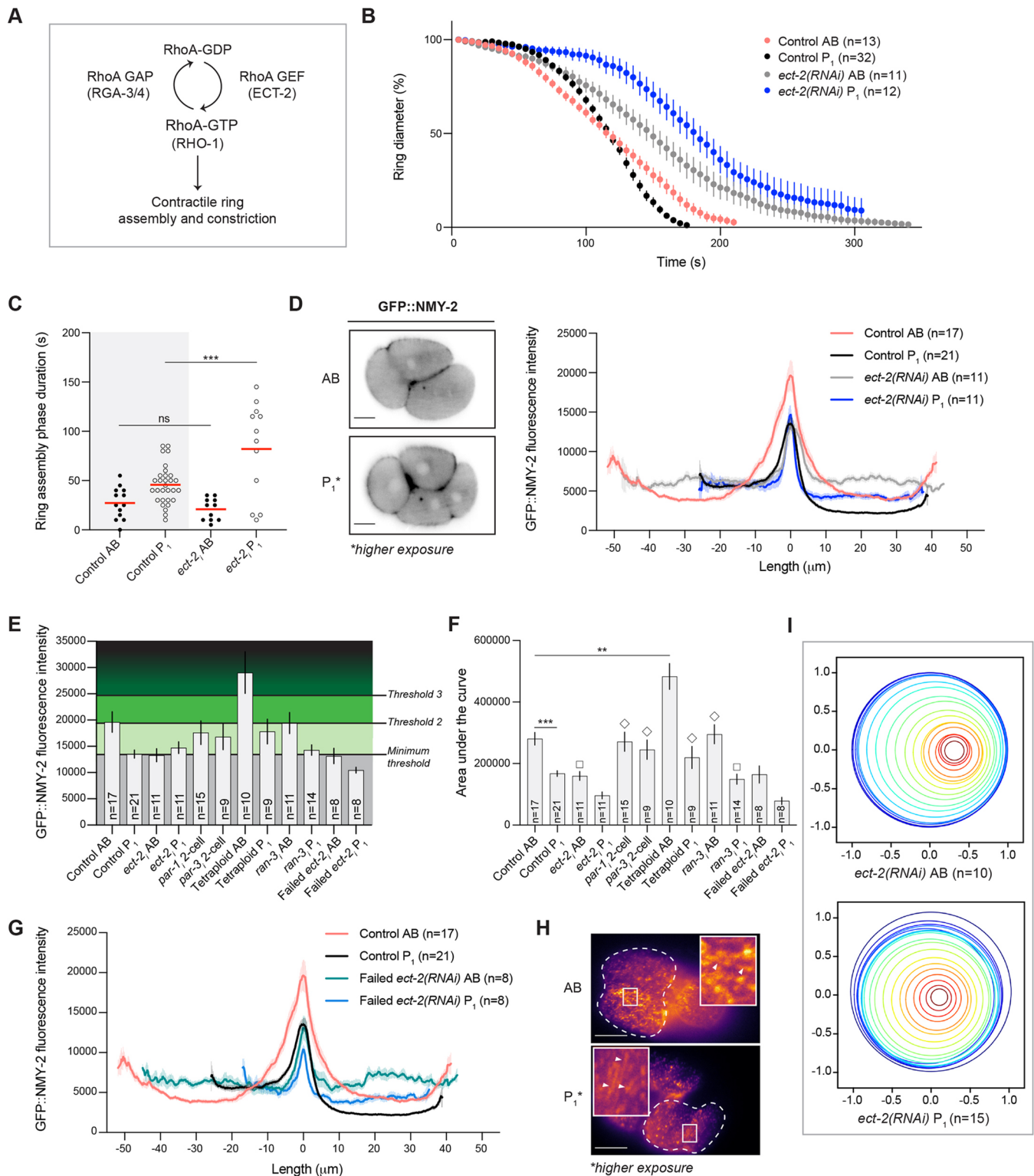


Fig. 2. Cytokinesis still occurs uniquely in AB and P₁ cells after perturbing actomyosin contractility. (A) The RhoA pathway for contractile ring assembly is shown. (B) A graph shows ring closure in *ect-2(RNAi)* AB and P₁ cells compared to control cells. (C) A plot shows the duration of ring assembly for individual cells (mean, red lines; ns, not significant; ***P<0.001; two-way ANOVA). (D) Left: inverted images show GFP::NMY-2 localization in *ect-2(RNAi)* AB and P₁ cells. Right: GFP::NMY-2 levels at the midplane cortex are shown for control and *ect-2(RNAi)* AB and P₁ cells that complete cytokinesis. (E) A graph shows the maximum GFP::NMY-2 intensity values in the furrow of cells under different conditions. The distinct myosin threshold levels for ring assembly are indicated by different shades of green. (F) Accumulated myosin based on area under the peak region of the curve from cells in E (**P<0.01; ***P<0.001; diamonds, not significant versus control AB; squares, not significant versus control P₁; Welch's t-test). (G) GFP::NMY-2 intensity in *ect-2(RNAi)* AB and P₁ cells that fail cytokinesis is shown as in D. (H) Pseudocolored HILO images show GFP::NMY-2 in a dividing *ect-2(RNAi)* AB and P₁ cell (outlined by dashed line). Arrowheads in the zoomed images (boxes) point to myosin filament bundles. (I) End-on views of ring closure are shown over time, with each timepoint as a different color. X- and y-axes indicate ratios of the distance from the starting position (0). Scale bars: 10 μm. Data in B and D–G are expressed as mean±s.e.m.

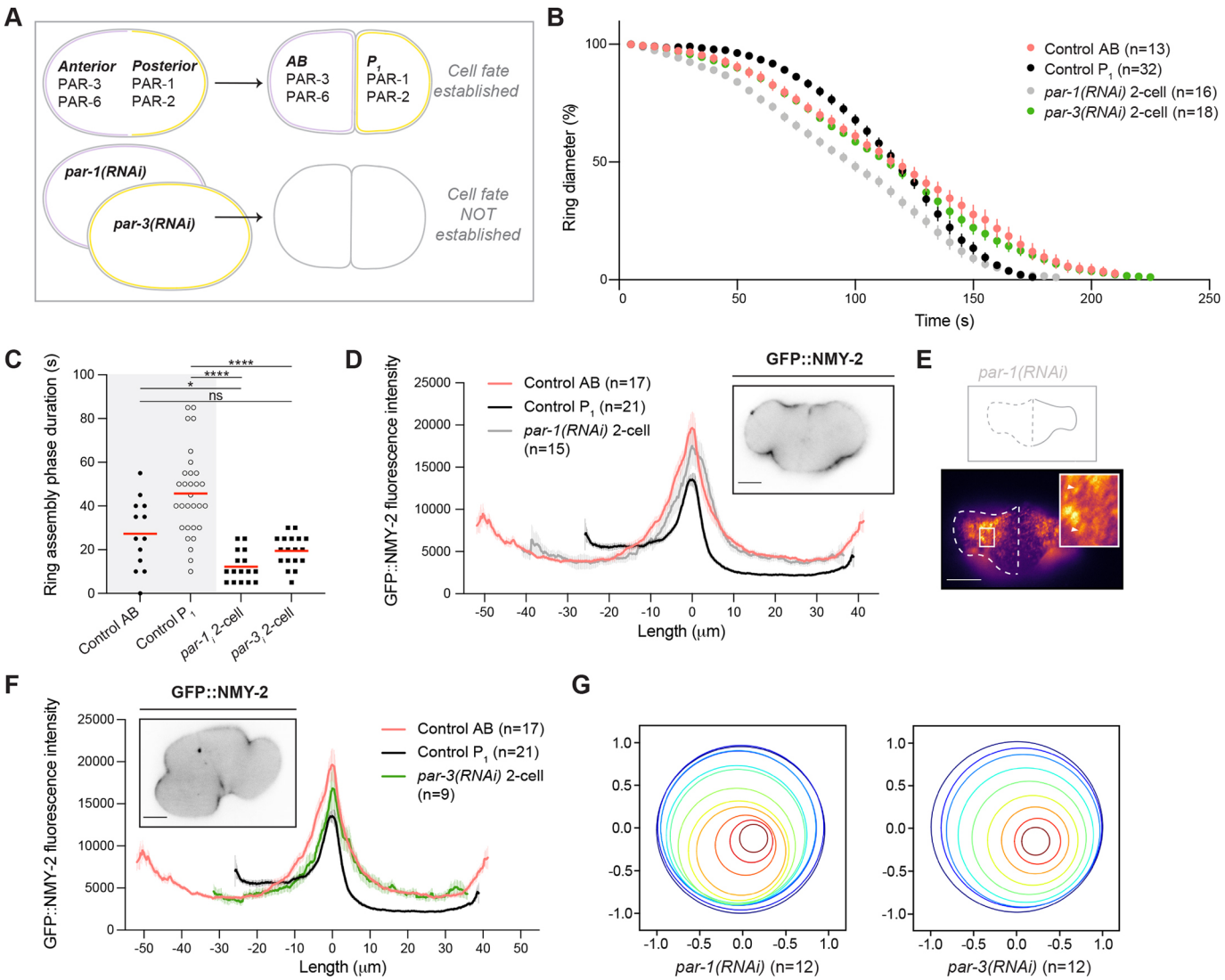


Fig. 3. Differences in ring assembly between AB and P_1 cells are fate dependent. (A) Cartoons show the distribution of PAR proteins in the P_0 zygote, and how their depletion disrupts cell fate. (B) A graph shows ring closure in $par-1(RNAi)$ and $par-3(RNAi)$ P_0 daughters compared to control. (C) A plot shows the duration of ring assembly for individual cells (mean, red lines; * $P \leq 0.05$; **** $P \leq 0.0001$; ns, not significant; Welch's t -test). (D) GFP::NMY-2 levels at the midplane cortex are shown for $par-1(RNAi)$ P_0 daughter cells compared to control. GFP::NMY-2 localization is shown in the inset. (E) Pseudocolored HILo images show GFP::NMY-2 in a dividing $par-1(RNAi)$ P_0 daughter cell (dashed outline). Arrowheads in the zoomed image (box) point to myosin filament bundles. (F) GFP::NMY-2 levels are shown as in D for $par-3(RNAi)$ P_0 daughter cells. (G) End-on views of ring closure are shown over time, where each timepoint is a different color. X- and y-axes indicate ratios of the distance from the starting position (0). Scale bars: 10 μm . Data in B, D and F are expressed as mean \pm s.e.m.

Cell size and ploidy influence the rate of ring assembly

We also determined how ring assembly was affected by changing cell size and ploidy. We generated tetraploid (4n) mNeonGreen::PH; mCherry::HIS-58 embryos, which have a 1.3-fold and 1.5-fold increase in AB (27–35 μm) and P_1 (18.1–27.2 μm) cell size, respectively (Table 1, Fig. 4A; Fig. S1D). The average size of tetraploid P_1 cells is nearly identical to diploid AB cells, and the cells retain their appropriate fates. The ring assembly phase was similar in tetraploid P_1 and diploid AB cells (Fig. 4B,C), but took much longer in tetraploid AB cells compared to diploid AB or P_1 cells (Fig. 4B,C). The unexpected delay in ring assembly in tetraploid AB cells prompted us to determine whether there is a relationship between ring assembly and cell size in AB and P_1 cells. First, we compared the duration of each phase with cell size in control diploid cells. We used simple linear regression and found that there was no correlation between ring assembly and cell size in diploid AB cells, whereas P_1 cells had a negative correlation regardless of the sample size,

suggesting that rings take longer to assemble in the smaller P_1 cells (Fig. 4D; Fig. S6A). We observed different trends during the other phases when actomyosin filaments transition to force generation.

Table 1. Mean size of cells in the two-cell embryo across different conditions		
	Mean size (μm)	s.e.m.
Control AB	26.97	0.59
Control P_1	18.14	0.33
<i>ect-2(RNAi)</i> AB	26.66	0.38
<i>ect-2(RNAi)</i> P_1	21.72	0.77
<i>par-1(RNAi)</i>	23.53	0.62
<i>par-3(RNAi)</i>	28.58	0.39
Tetraploid AB	35.00	0.51
Tetraploid P_1	27.21	0.78
<i>ran-3(RNAi)</i> AB	22.53	0.98
<i>ran-3(RNAi)</i> P_1	21.82	0.45

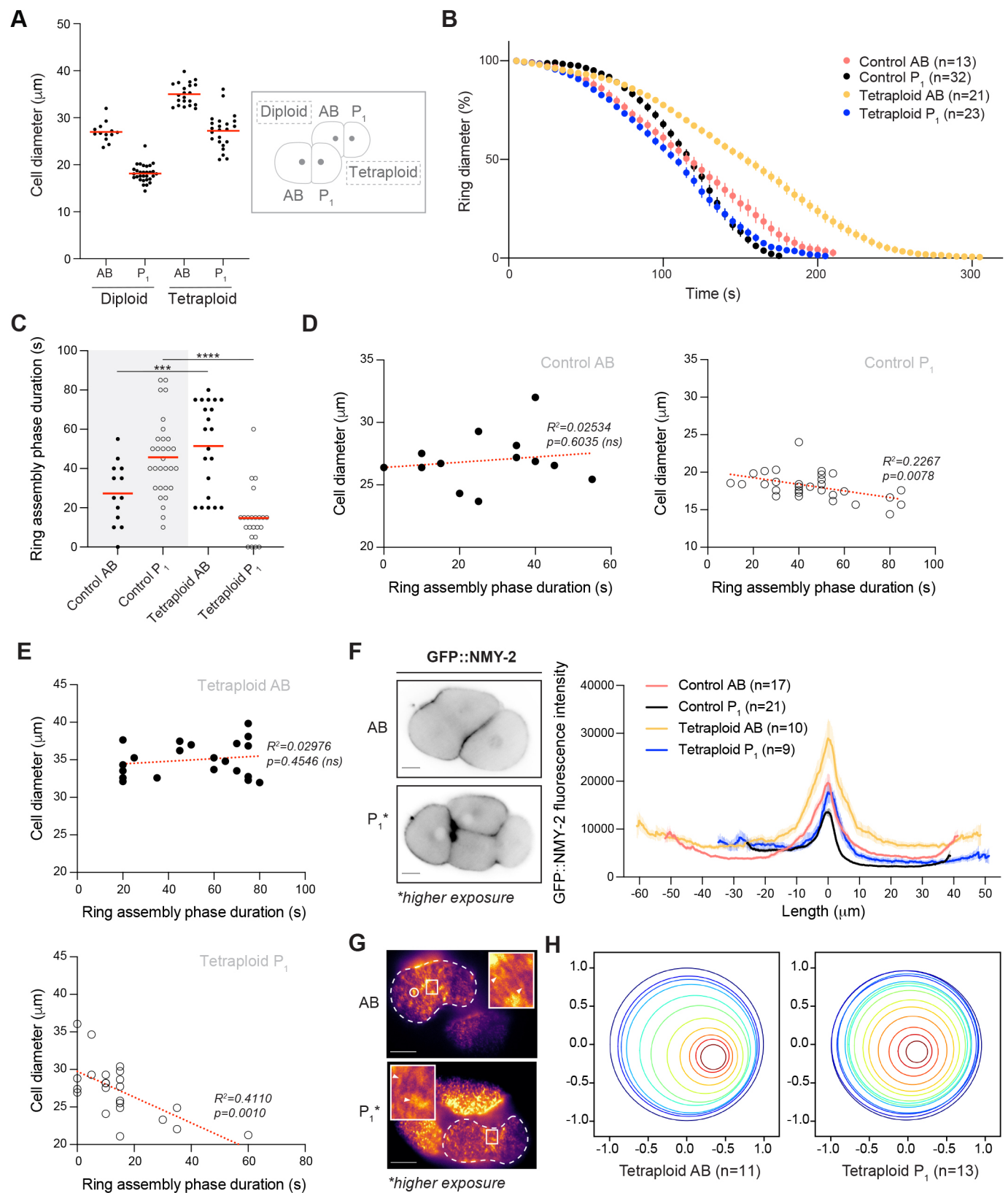


Fig. 4. See next page for legend.

Whereas furrow initiation showed a positive correlation with size in P_1 cells and no correlation in AB cells, both cell types had a positive correlation with size during ring closure (Fig. S6B). We were surprised to see that larger cells took longer to constrict, which is

contradictory to a previously published study showing that constriction rates positively correlate with size. However, the previous study explored cells with greater differences in size compared to this study, where cells are closer in range and could

Fig. 4. Cell size and ploidy contribute to differences in ring assembly between AB and P₁ cells. (A) Left: a plot shows the size of diploid and tetraploid AB and P₁ cells (mean, red lines). Right: cartoons highlight their relative sizes. (B) A graph shows ring closure in tetraploid AB and P₁ cells compared to control; *n* values include 21 sister pairs. (C) A plot shows the duration of ring assembly for individual cells (mean, red lines; ****P*≤0.001; *****P*≤0.0001; two-way ANOVA). (D,E) Graphs show the correlation between ring assembly and cell diameter for control AB and P₁ cells (D) and for tetraploid AB and P₁ cells (E). Red dotted lines show simple linear regression (*R*² and *P* are shown; ns, not significant). (F) Left: inverted images show GFP::NMY-2 localization in tetraploid AB and P₁ cells. Right: GFP::NMY-2 levels at the midplane cortex of tetraploid AB and P₁ cells are shown compared to control. (G) Pseudocolored HILO images show GFP::NMY-2 in a tetraploid AB and P₁ cell (dashed line). The circle shows a myosin cluster. Arrowheads in the zoomed image (box) point to myosin filament bundles. (H) Ring closure is shown over time, with each timepoint as a different color. X- and y-axes indicate ratios of the distance from the starting position (0). Scale bars: 10 μm. Data in B and F are expressed as mean±s.e.m.

reflect differences within versus between different size scales. Next, we determined whether there was a correlation with cell size and duration of ring assembly after depletion of ECT-2, PAR-1 or PAR-3 (Fig. S6C,D). There was no correlation in AB cells as expected, but the correlation was lost in P₁ cells in all treatments, suggesting that this depends on actomyosin levels and cell fate (Fig. S6C,D). In support of this, there was no correlation between ring assembly and size in tetraploid AB cells, whereas a stronger negative correlation was observed in tetraploid P₁ cells (Fig. 4E). The strong negative correlation in tetraploid P₁ cells supports the hypothesis that the factors controlling ring assembly in response to size are fate dependent. As tetraploid cells have higher ploidy, it is possible that these factors include Ran signaling, which relies on inverse Ran-GTP and importin gradients formed by chromatin (Hasegawa et al., 2013).

To determine whether the different ring assembly kinetics in tetraploid AB and P₁ cells correlates with myosin levels and/or organization, we generated tetraploid embryos expressing GFP::NMY-2. Peak myosin levels in tetraploid AB cells were 48% higher and more broadly distributed compared to diploid AB cells (Figs 2E and 4F). There was also a 32% increase in peak myosin levels in tetraploid P₁ cells such that they were comparable to control AB cells (Figs 2E and 4F). The same results were obtained regardless of whether AB or P₁ cells from the same or different embryos were analyzed (Fig. S3E). Accumulated myosin in the furrow region was also higher in tetraploid AB cells, and tetraploid P₁ cells were comparable to diploid AB cells (Fig. 2F). HILO imaging revealed a high number of myosin clusters in tetraploid AB cells, with densely packed, well-aligned filament bundles throughout the cortex (Fig. 4G; Movie 6). Tetraploid P₁ cells also appeared to have a greater density of myosin compared to diploid P₁ cells (Fig. 4G; Movie 6). The slower kinetics in tetraploid AB cells could be due to excessive force generation outside the furrow region. Surprisingly, we also found that rings closed asymmetrically in tetraploid P₁ cells, similar to diploid AB cells (Fig. 4H; Fig. S3D). Our results suggest that distinct thresholds of myosin support different kinetics, and high levels can hinder ring assembly. These data also suggest that ideal levels of myosin can override the factors that delay ring assembly in P₁ cells.

The Ran pathway regulates cytokinesis differently in AB and P₁ cells

Our data show that multiple mechanisms regulate contractile ring assembly. We recently found that the Ran pathway controls ring position in response to chromatin in HeLa cells, and our model is that importin binding to NLS-containing cortical proteins positively

regulates their recruitment and/or function at the equatorial cortex (Beaudet et al., 2017, 2020). The Ran pathway has not been studied in many cell types and its requirement could vary with cell size, ploidy and fate. First, we determined whether Ran regulates cytokinesis in AB and P₁ cells. We partially depleted RAN-3 (RCC1) to decrease the levels of Ran-GTP and increase the pool of importins that can bind to NLS-containing proteins (Fig. 5A). We observed equalized kinetics in *ran-3(RNAi)* AB and P₁ cells, which both had shorter ring assembly phases compared to control cells (Fig. 5B,C; Fig. S1E). A comparison of other phase durations showed that furrow initiation was not altered in *ran-3(RNAi)* AB and P₁ cells, whereas constriction was faster for AB cells and slower for P₁ cells (Fig. S7A). Interestingly, we also saw no correlation between cell size and the duration of ring assembly in *ran-3(RNAi)* AB or P₁ cells (Fig. S6E). In addition to changes in cytokinesis, we observed a prophase delay in *ran-3(RNAi)* P₁ cells, which increased the heterochronicity between AB and P₁ divisions. We used this delay as a visible marker to follow the efficiency of *ran-3(RNAi)* knockdown. We also observed that AB and P₁ cells were similar in size (Table 1). To ensure that the *ran-3(RNAi)* phenotypes were not caused by a change in polarity, we imaged embryos co-expressing GFP::PH with PGL-1::RFP, which is a marker of P granules (Fig. S7B). We saw that P granules segregated asymmetrically to P₁ and P₂ cells in embryos after *ran-3(RNAi)*, similar to control embryos (Strome and Wood, 1982). We also considered that *ran-3(RNAi)* could cause spindle defects, because changes in Ran-GTP levels can affect spindle assembly (e.g. Schatz et al., 2003). However, as we only measured cytokinesis in *ran-3(RNAi)* cells where chromosomes segregated, we did not think that our RNAi treatment was severe enough to cause spindle defects. We verified this by imaging embryos co-expressing mCherry::HIS-58, GFP::PH and GFP::TBB-2 to visualize microtubules, and indeed spindle length was similar between control and *ran-3(RNAi)* AB and P₁ cells (Fig. S7C).

Next, we determined whether the rapid ring assembly kinetics in *ran-3(RNAi)* cells was caused by an increase in myosin levels and/or organization. Peak myosin levels and total accumulation of myosin in the furrow region of *ran-3(RNAi)* AB or P₁ cells showed no significant change (Figs 2E,F and 5D). As myosin levels are not sufficient to support the faster kinetics in P₁ cells, we also characterized the appearance of the filaments. HILO imaging revealed that both AB and P₁ cells had densely packed filamentous myosin, and AB cells had strong cortical flows (Fig. 5E; Movies 7 and 8). In support of their rapid kinetics, the myosin filament bundles appeared to be well aligned in both AB and P₁ *ran-3(RNAi)* cells, but particularly in P₁ cells compared to control. These results suggest that decreasing the levels of Ran-GTP enhances the organization of actomyosin filaments. Interestingly, we also observed that rings closed asymmetrically in both AB and P₁ cells after RAN-3 depletion (Fig. 5F; Fig. S3D).

Next, we determined whether the faster kinetics in *ran-3(RNAi)* AB and P₁ cells are a result of RhoA-mediated contractility. Partial depletion of ECT-2 partially suppressed the rapid ring assembly kinetics caused by RAN-3 depletion in AB and P₁ cells (Fig. 5G,H), with the caveat that the ring assembly phase is more challenging to define in *ect-2(RNAi)* cells. Therefore, decreasing active RhoA and contractility could counter the increase in contractility caused by decreasing Ran-GTP.

Ran regulation occurs through different components in AB and P₁ cells

Next, we determined whether Ran influences ring assembly by regulating importins. To do this, we depleted IMA-3 (importin-α) or

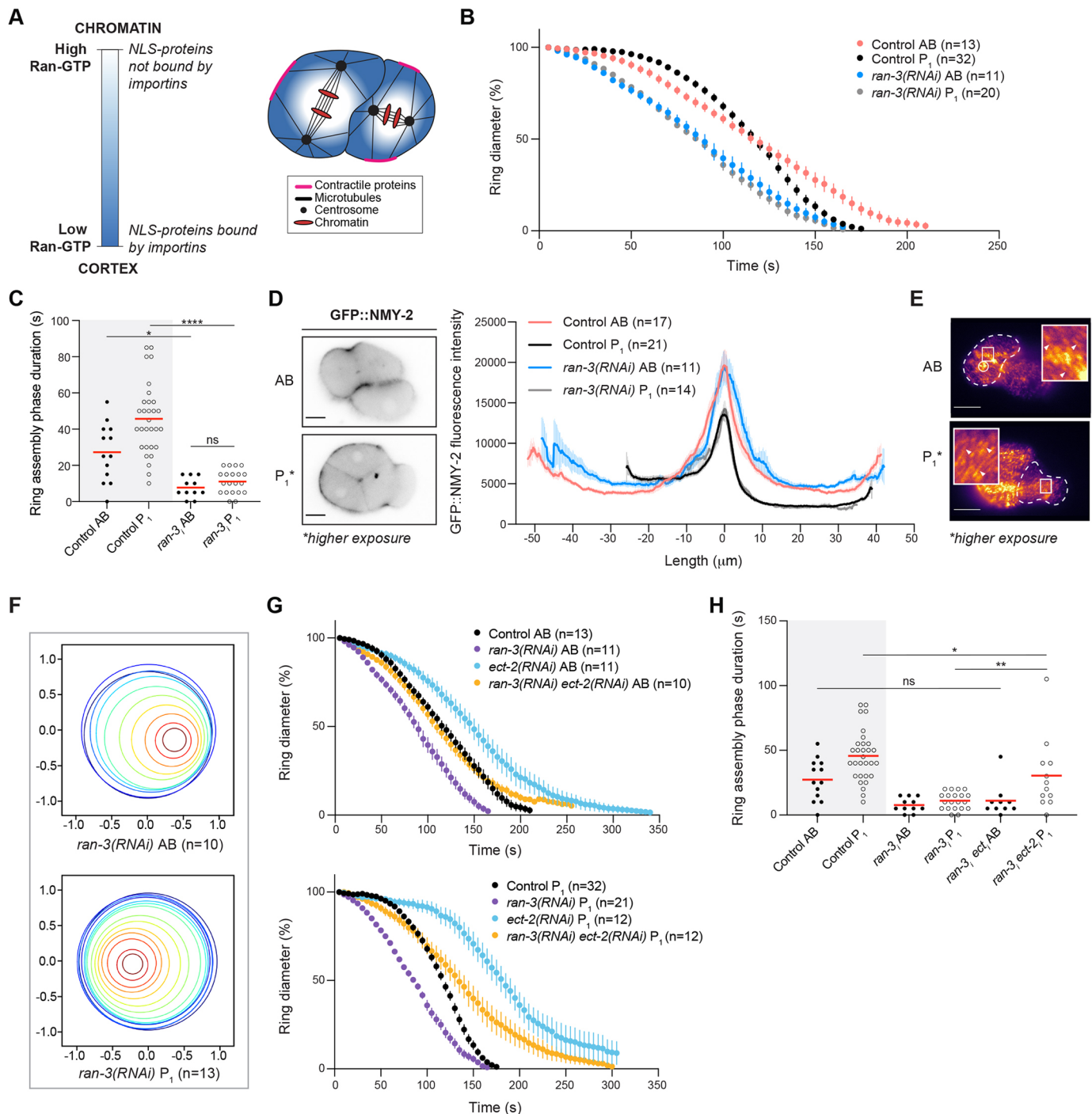


Fig. 5. Ran regulates ring assembly in AB and P₁ cell cytokinesis. (A) A cartoon shows the importin gradient in the two-cell embryo. Ran-GTP is high near chromatin and low near the cortex where importins are free to bind to NLS-containing cortical proteins. (B) A graph shows ring closure in *ran-3(RNAi)* AB and P₁ cells compared to control. (C) A plot shows the duration of ring assembly for individual cells (mean, red lines). (D) Left: inverted images show GFP::NMY-2 localization in *ran-3(RNAi)* AB and P₁ cells. Right: GFP::NMY-2 levels at the midplane cortex of *ran-3(RNAi)* AB and P₁ cells are shown compared to control. (E) Pseudocolored HILO images show GFP::NMY-2 in a dividing *ran-3(RNAi)* AB and P₁ cell (outlined by dashed line). The circle shows a myosin cluster. Arrowheads in the zoomed image (box) point to myosin filament bundles. (F) Ring closure is shown over time, with each timepoint as a different color. X- and y-axes indicate ratios of the distance from the starting position (0). (G) Graphs show ring closure in AB and P₁ *ran-3(RNAi)*, *ect-2(RNAi)* and *ran-3(RNAi) ect-2(RNAi)* cells compared to control. (H) A plot shows the duration of ring assembly for individual cells (mean, red lines). Scale bars: 10 μm. Data in B, D, G are expressed as mean±s.e.m. For C and H, **P*≤0.05, ***P*≤0.01, *****P*≤0.0001; ns, not significant; two-way ANOVA.

IMB-1 (importin-β). *C. elegans* has three importin-α homologs (IMA-1, -2 and -3), but IMA-1 depletion has no obvious phenotype, and IMA-2 is essential for spindle assembly precluding its use in this study (Geles and Adam, 2001; Askjaer et al., 2002).

Interestingly, whereas *ima-3(RNAi)* caused faster ring assembly in both AB and P₁ cells, *imb-1(RNAi)* caused faster assembly only in P₁ cells (Fig. 6A). *ima-3(RNAi)* also causes embryos to be smaller in size, which allowed us to follow knockdown efficiency.

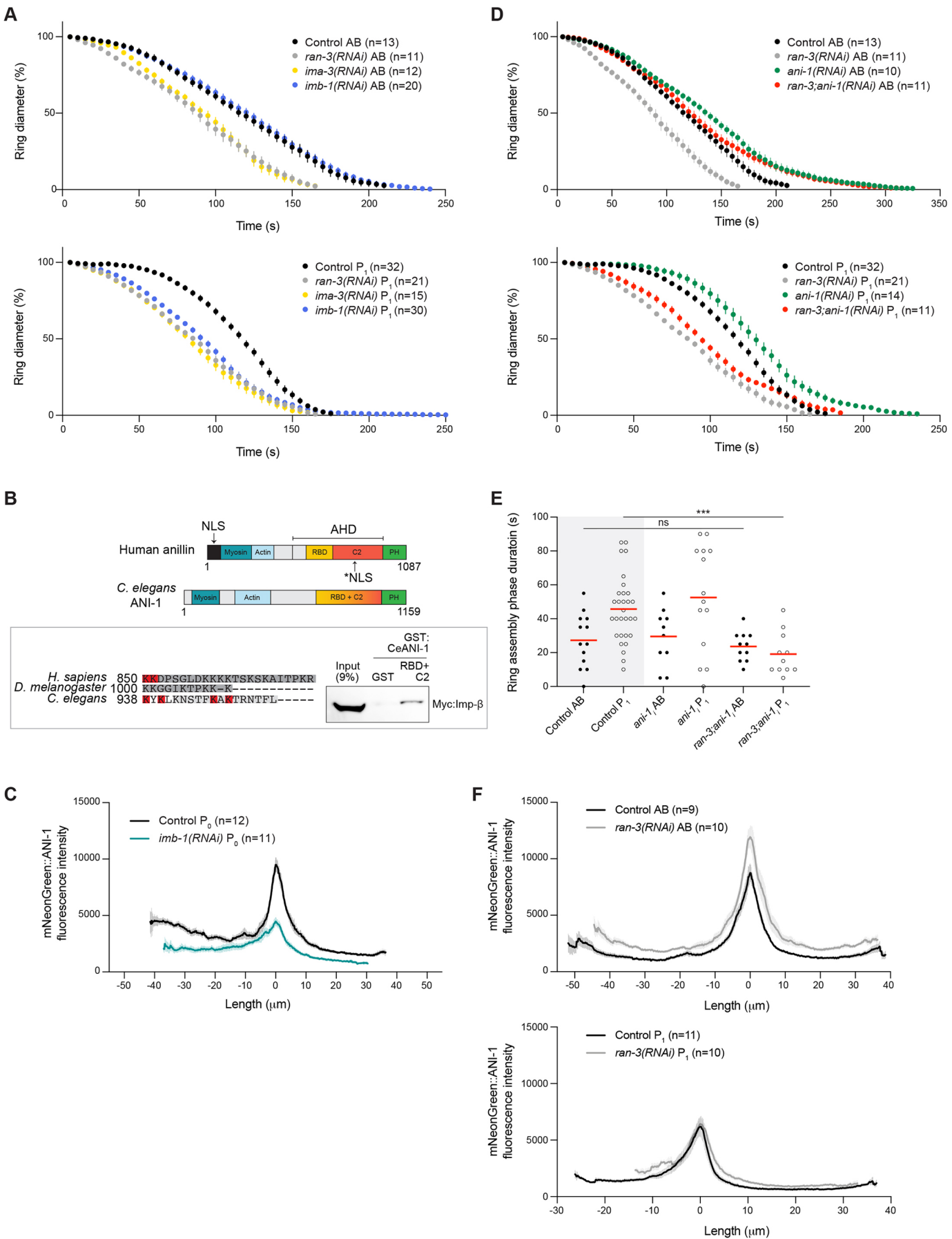


Fig. 6. See next page for legend.

Fig. 6. Ran differently regulates ring assembly in AB and P₁ cells.

(A) Graphs show ring closure in AB and P₁ *ran-3(RNAi)*, *ima-3(RNAi)* and *imb-1(RNAi)* cells compared to control. (B) Top: schematics show the structures of human anillin and *C. elegans* ANI-1 (Myosin, myosin binding domain; Actin, F-actin binding domain; RBD, RhoA-GTP binding domain; C2, C2 domain; PH, pleckstrin homology domain; AHD, anillin homology domain). NLS sites are shown in human anillin; the asterisk indicates the site required for cytokinesis. Bottom left: the C-terminal NLS is shown for anillin homologs; residues required for importin binding are in red. Bottom right: a western blot shows Myc-tagged importin- β from HeLa cell lysates (input) and after pull down with recombinant, purified GST or GST-tagged ANI-1 (RBD+C2). Blot shown is representative of three experiments. (C) mNeonGreen::ANI-1 levels at the midplane cortex are shown for *imb-1(RNAi)* P₀ cells compared to control. (D) Graphs show ring closure in AB and P₁ *ran-3(RNAi)*, *ani-1(RNAi)* and *ran-3(RNAi); ani-1(RNAi)* cells compared to control. (E) A plot shows the duration of ring assembly for individual cells (mean, red lines; *** $P \leq 0.001$; ns, not significant; two-way ANOVA). (F) mNeonGreen::ANI-1 levels at the midplane cortex are shown for control and *ran-3(RNAi)* AB and P₁ cells. Data in A, C, D and F are expressed as mean \pm s.e.m.

Co-depletion of IMB-1 suppressed the rapid ring assembly caused by IMA-3 in AB cells, but only partially suppressed assembly in P₁ cells (Fig. S7D). This differential response suggests that there are different threshold requirements for the different importins in AB and P₁ cells, with the caveat that this could reflect differences in RNAi efficiency. One interpretation is that IMB-1 influences ring assembly in AB cells, but not IMA-3, whereas in P₁ cells IMA-3, IMB-1 and/or the heterodimer can influence ring assembly.

We then determined whether ANI-1 (anillin) is a target of the Ran pathway in AB and P₁ cells. Currently, anillin is the only cytokinesis protein known to be regulated by importin- β -binding for its cortical function in human cells. ANI-1 shares homology with human anillin (Fig. 6B, top), and the NLS in the C2 domain is somewhat conserved (Fig. 6B, bottom left). Indeed, GST-tagged ANI-1 [RhoA-GTP binding domain (RBD)+C2] pulled down Myc-tagged human importin- β from cell lysates (Fig. 6B, bottom right). This binding was reduced by point mutations in the NLS (Fig. S7E). As further support for the importin regulation of ANI-1, we observed a decrease in the midplane levels of mNeonGreen-tagged ANI-1 in the furrow region of P₀ cells in *imb-1(RNAi)* embryos (Fig. 6C). Collectively, these data suggest that ANI-1 could be regulated by importin binding and the Ran pathway in *C. elegans*. To determine whether lowering Ran-GTP levels causes rapid ring assembly by facilitating ANI-1 function, we co-depleted RAN-3 and ANI-1. In *ani-1(RNAi)* embryos, the early phases of cytokinesis were similar or slightly delayed compared to control AB and P₁ cells (Fig. 6D,E). Interestingly, ANI-1 depletion suppressed the rapid assembly kinetics caused by RAN-3 depletion in AB, but not P₁, cells (Fig. 6D,E). To ensure that ANI-1 was sufficiently depleted, we followed the large polar body phenotype, and measured ANI-1 levels in single and double knockdown embryos (Fig. S7F). To determine whether ANI-1 could be regulated by RAN-3 in AB cells, we measured changes in ANI-1 localization in *ran-3(RNAi)* embryos. Indeed, although peak ANI-1 levels increased in *ran-3(RNAi)* AB cells relative to control, they remained unchanged in P₁ cells (Fig. 6F). These data support that the Ran pathway regulates the cortical recruitment of ANI-1 for the equatorial organization of actomyosin filaments in AB cells. However, the pathway functions differently in the germline precursor P₁ cells and involves different targets.

DISCUSSION**AB and P₁ cells have distinct cytokinesis kinetics**

We demonstrate that AB and P₁ cells in the *C. elegans* embryo have unique ring assembly kinetics, which reflect differences in

actomyosin levels and mechanisms affecting their organization. We found that the ring assembly phase is faster in AB cells compared to P₁ cells, which correlates with higher levels of equatorial myosin and aligned filament bundles that appear to flow into the contractile ring (Fig. 1). This is consistent with previous studies suggesting that long-range flows promote ring assembly (Singh and Pohl, 2014; Reymann et al., 2016; Khaliullin et al., 2018; Illukkumbura et al., 2020). Additionally, the clusters that form in the AB cortex could facilitate the alignment and organization of actomyosin and/or compression (Reymann et al., 2016; Khaliullin et al., 2018). We also observed asymmetric closure of the ring in AB cells towards the AB–P₁ cell boundary, in line with previous reports (Maddox et al., 2007; Bai et al., 2020). This closure is required to position the midbody to align the spindle in the P₁ cell. However, the mechanisms driving asymmetric closure of AB cells are not well understood. In contrast, actomyosin takes longer to accumulate in P₁ cells, which lack cortical flows and have less cortical myosin, and ring constriction occurs with less hindrance due to lower cortical tension that antagonizes furrowing (Silva et al., 2016). These data indicate that the levels of myosin and their organization correlate with the observed kinetics in the two cell types (Figs 2E,F and 7A). Partial depletion of ECT-2, which generates active RhoA for actomyosin filament assembly (Green et al., 2012), revealed that AB cells are sensitized to cytokinesis failure when myosin levels drop closer to those typically found in control P₁ cells, which operate closer to the minimum threshold (Fig. 2D–F). Rings still closed asymmetrically in *ect-2(RNAi)* AB cells, although they were more symmetrical compared to control, suggesting the contribution of multiple factors. Another surprising finding was that the rate of ring assembly remained AB-like in AB cells after partial depletion of NMY-2 or ECT-2 (Fig. 2B; Fig. S3C). This result shows that multiple factors control ring assembly, which could be differently partitioned between AB and P₁ cells.

Differences in AB and P₁ ring assembly are fate dependent

Disrupting cell fate by depleting PAR-1 or PAR-3 equalized ring closure kinetics between the daughter cells, which had short ring assembly phases similar to control AB cells (Fig. 3). PAR-1 and PAR-3 are part of posterior and anterior complexes, respectively, which reinforce anterior-enriched cortical contractility (Cowan and Hyman, 2007; Hoege and Hyman, 2013; Rose and Gonczy, 2014; Gan and Motegi, 2020). We expected different kinetics after depletion of PAR-1 or PAR-3; however, the loss of either PAR caused cells to be more AB-like, with myosin levels between AB and P₁ cells, and swaths of well-aligned filament bundles (Figs 2E,F, 3E and 7A). It is not clear why PAR-3 depletion caused AB-like kinetics. Multiple factors regulate global cortical contractility in oocytes, which is inhibited at the posterior cortex by PAR-1–PAR-2, and expansion of this complex may be insufficient to entirely suppress these factors (Cowan and Hyman, 2007; Hoege and Hyman, 2013; Rose and Gonczy, 2014; Gan and Motegi, 2020). Also, this early pool of contractile myosin would be distributed equally to the daughters.

Size and ploidy govern differences in AB and P₁ ring closure kinetics

Cell size also influences the duration of ring assembly in P₁, but not AB, cells. We observed a negative correlation between size and the duration of ring assembly in P₁ cells (Fig. 4D), meaning that rings assemble more quickly in larger cells. One hypothesis is that the Ran-GTP gradient extends closer to the cortex in smaller cells, where it could inhibit contractile ring assembly. This hypothesis is

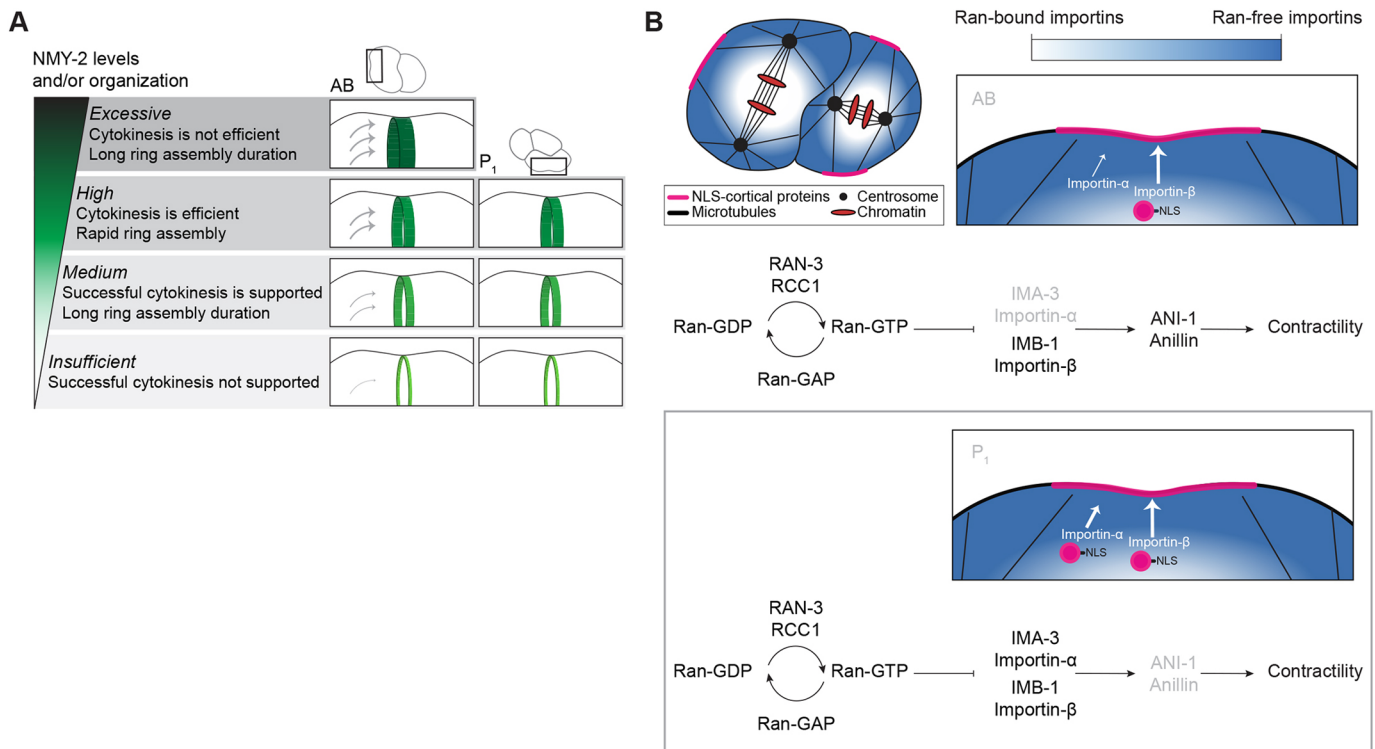


Fig. 7. Myosin levels and organization in addition to the pathways of regulation contribute to differences in cytokinesis. (A) A schematic shows the correlation between the thresholds of myosin, ring assembly and cytokinesis efficiency. The contractile ring is in green, myosin levels are in shades of green, and arrows indicate flows. (B) Cartoons show different requirements for the Ran pathway in AB and P₁ cells (black font, high; gray font, low). The gradient of importins free to bind to NLS-containing cortical proteins (NLS-cortical proteins) is shown relative to chromatin.

supported by the loss of correlation between cell size and ring assembly in *ran-3(RNAi)* embryos (Fig. S6E). In this model, higher levels of importins free to bind to cortical NLS-containing proteins would promote ring assembly in larger cells, whereas lower levels prevent efficient assembly in smaller cells. A non-mutually exclusive hypothesis is that a larger P₁ cell could reflect a larger inheritance of actomyosin compared to a smaller P₁ cell because of a more symmetric P₀ division. Since P₁ cells already operate at thresholds of myosin close to what is required to support division, even minor increases in myosin or its regulators could facilitate ring assembly more easily, despite their increase in size. Both models could apply to tetraploid P₁ cells, which displayed a shorter ring assembly phase similar to control AB cells, yet still showed a negative correlation between ring assembly and size (Fig. 4C,E). We observed higher levels of myosin in tetraploid P₁ cells compared to control P₁ cells, which could more readily facilitate ring assembly (Fig. 4F). This finding supports that increasing actomyosin can override the delays in ring assembly in P₁ cells, but the mechanisms controlling ring assembly in P₁ cells, such as the Ran pathway, can still respond to size differences. The negative correlation with ring assembly and size was lost in *ect-2(RNAi)*, *par-1(RNAi)* and *par-3(RNAi)* embryos (Fig. S6C,D). Although myosin levels could be too low to support a correlation in *ect-2(RNAi)* cells, the loss of cell identity after PAR depletion would remove any cell-specific correlations. After ring assembly, we observed positive correlations with size and furrow initiation and constriction phases in P₁ cells, and with constriction in AB cells (Fig. S6B). These results indicate a switch where larger cells take longer to furrow or ingress, suggesting that it is harder to generate the force needed to overcome tension in the larger cells. Although our findings appear to be somewhat contradictory to what was previously published, this prior study

explored vastly different cell sizes, and the idea that rings have structural memory to coordinate division during development could still apply in a broader context (Carvalho et al., 2009).

The Ran pathway regulates cytokinesis differently in AB and P₁ cells

We found that the Ran pathway controls ring assembly and functions differently in AB and P₁ cells (Fig. 7B). Our studies of cytokinesis in HeLa cells showed that Ran-GTP coordinates the position of the contractile ring with segregating chromosomes, and we propose that the requirement for this mechanism could vary with cell size, ploidy or fate (Beaudet et al., 2017, 2020). A gradient of active Ran associated with chromatin forms inverse to a gradient of importins free to bind to NLS-containing proteins (Ozugergin and Piekny, 2021). Although importin binding negatively regulates spindle assembly factors, we propose that it positively regulates cortical proteins for cytokinesis, such that the same gradient has reciprocal functions near chromatin versus near the cortex (Ozugergin and Piekny, 2021). Importantly, the Ran-importin gradient was shown to vary with size and ploidy in various cell types and contexts (Deng et al., 2007; Hasegawa et al., 2013). Human anillin contains an NLS that binds to importin-β and is required for its localization and function during cytokinesis (Beaudet et al., 2017, 2020). This NLS is conserved in ANI-1, and binding to importin-β could similarly facilitate its cortical recruitment during cytokinesis (Fig. 6B,C; Fig. S7E). Lowering Ran-GTP levels equalized kinetics in AB and P₁ cells, which had a faster ring assembly phase compared to control cells (Fig. 5). This change in kinetics was not a result of changes in myosin levels, but rather improved myosin organization, which could generate stronger forces for filament alignment (Fig. 5D–F). Additionally, we found

that ANI-1 is a target of the Ran pathway in AB but not P₁ cells (Figs 6D–F and 7B), and we are currently identifying NLS proteins that are regulated by this pathway.

We also found that different components of the Ran pathway have different threshold requirements in AB and P₁ cells. Ring assembly was faster in both cells after IMA-3 depletion, but only in P₁ cells after IMB-1 depletion (Fig. 6A). The dogma is that importin- α binds to the NLS of proteins and acts as an adaptor protein for importin- β (Xu and Massague, 2004; Ozugergin and Piekny, 2021). However, data from multiple labs suggest that importins can bind independently or as a heterodimer (e.g. Chan and Jans, 1999; Gruss et al., 2001; Schatz et al., 2003; Silljé et al., 2006; Giesecke and Stewart, 2010; Ozugergin and Piekny, 2021). As the depletion of either importin led to faster kinetics in P₁ cells, we propose that either IMA-3 or IMB-1 can regulate cortical proteins for cytokinesis in these cells (Fig. 7B). However, our data support that IMB-1 might play a stronger role in AB cell ring assembly, as IMA-3 depletion could release more IMB-1 to bind to ANI-1 and facilitate faster kinetics.

Our findings build on studies of cytokinesis in the four-cell *C. elegans* embryo demonstrating that cells have different levels of F-actin regulated by intrinsic or extrinsic mechanisms (Davies et al., 2018). These differences in F-actin reflect the differences in myosin that we observed in AB and P₁ cells, suggesting that they arise at the previous division. We also expand on this knowledge by demonstrating that filament organization correlates with ring assembly kinetics, and that the Ran pathway differently regulates ring assembly in AB versus P₁ cells. Why would AB and P₁ cells have different mechanisms that control ring assembly? AB cells are fated to give rise to multiple somatic tissues, whereas P₁ cells are fated to form the germline. Ring assembly may occur similarly in AB cells and somatic cells in other organisms. P cells might differ because they undergo several asymmetric divisions before daughters are born that fail cytokinesis and ultimately form the germline syncytium (Amini et al., 2014; Goupil et al., 2017; Bauer et al., 2021). Having less actomyosin and factors that control the timing of ring assembly in P cells could temporally coordinate the completion of cytokinesis with their neighboring somatic cell, which could be crucial for proper cell fate determination during embryogenesis.

MATERIALS AND METHODS

Strains

C. elegans strains (Table S1) were maintained according to standard protocols (Brenner, 1974) using nematode growth medium (NGM) plates. Control worms were grown on plates seeded with *Escherichia coli* OP50.

RNA interference

RNAi was carried out using feeding vectors for the induction of dsRNA expression in HT115 bacteria to target H39E23.1 (*par-1*), F28B3.8 (*imb-1*), F32E10.4 (*ima-3*), F54E7.3 (*par-3*), T19E10.1 (*ect-2*) and Y49E10.19 (*ani-1*) from the Ahringer library (Kamath et al., 2001). Strains were generously provided by Dr Labbé (IRIC, Université de Montréal) and Dr Roy (McGill University). Bacterial cultures were grown overnight in Luria broth (LB) with 100 μ g/ml ampicillin at 37°C, then diluted 1:100 and grown at 37°C for 7 h. The cultures were pelleted and resuspended in LB (100 μ l for *ran-3*, *par-1* and *-3*, 300 μ l for *ani-1* and *ima-3*, 400 or 500 μ l for *ect-2*, 1700 μ l for *imb-1*), and 50–100 μ l of each resuspension was seeded onto NGM plates containing 100 μ g/ml ampicillin and 1 mM IPTG. After being left to dry, 10–15 L4 hermaphrodites were placed onto each plate for 3 (*imb-1*), 24 (*par-1*, *par-3*, *ran-3*, *ect-2*) or 30 h (*ani-1*, *ima-3*). Feeding on *imb-1* RNAi plates was kept within a 3–5 h window, as severe DNA defects were observed after longer periods. Data from RNAi conditions were obtained from at least three separate days to control for variability and validate reproducibility of the data. The W02A2.6 clone (*rec-8*) was used to generate

tetraploid worms, as described by Clarke et al. (2018). Specifically, L4 stage hermaphrodites of the desired strain were placed on *rec-8* RNAi plates for 8–9 days at 15°C. Then, 20 L4 stage hermaphrodites were transferred to freshly induced plates. After another 7–9 days, hermaphrodites that appeared longer than control were individually transferred onto OP50 plates and maintained for successive generations by repeatedly selecting long worms. Embryos were confirmed to have higher ploidy by cell size, and staining chromosomes in fixed embryos.

Microscopy

C. elegans embryos were prepared for imaging using a standard stereomicroscope by dissecting gravid hermaphrodites in M9 buffer (40 mM Na₂HPO₄, 22 mM KH₂PO₄, 85 mM NaCl and 2 mM MgSO₄) and transferring embryos onto a freshly prepared 2% agarose pad (Evans, 2006). Images of embryos were acquired with the 100 \times /1.45 NA objective on an inverted Nikon Eclipse Ti microscope fitted with a LiveScan Swept Field scanner (Nikon), Piezo Z stage (Prior), Andor IXON 897 EMCCD camera, and 488 nm and 561 nm lasers, using NIS-Elements (version 4.0, Nikon) software. Central z-planes of 0.7 μ m for a total z-stack of 4 μ m were collected at 5 s intervals for kymograph analysis, and 0.5 μ m z-planes for a total stack of 20 μ m were collected at 20 s to measure myosin or actin midplane cortical levels, and ring closure symmetry. All images were saved as ND2 files.

HILO microscopy, a modified form of total internal reflection fluorescence (TIRF) (Tokunaga et al., 2008), was used to image the cortex of the AB and P₁ cells in embryos. Embryos were transferred to agarose pads, as described above. A subcritical incidence angle was used and adjusted until clear images of the cortex were obtained. Images were acquired with a 100 \times /1.49 NA CFI Apo TIRF objective on an inverted Nikon Eclipse Ti microscope fitted with a TIRF arm, Photometrics Prime BSI (sCMOS) camera and 488 nm laser using NIS Elements (version 4.0, Nikon) software. Z-planes of 0.2 μ m for a z-stack of 0.6 μ m were collected at 2 s intervals. Images were saved as ND2 files.

Image analysis

Only cells that successfully completed cytokinesis and had proper DNA segregation with no gross morphological defects were used for analysis, with the exception of a subset of *ect-2(RNAi)* AB or P₁ cells that failed cytokinesis as described earlier. All raw data ND2 files were processed and/or analyzed in FIJI (version 2.1, NIH).

To determine the kinetics of ring closure, we used a custom macro written for FIJI to generate kymographs. Time-lapse images were staged to anaphase onset based on chromosome position (mCherry-tagged histone imaged via the 561 laser), and then the change in membrane position (mNeonGreen or GFP-tagged, imaged via the 488 laser) was analyzed over time. To generate kymographs, the image channels were split and the green (membrane) channel was retained to manually draw a line with a width of 5 pixels over the furrow region at every timepoint until closure. Then, the distance between the two sides of the membrane was measured at each timepoint using the straight-line tool, and measurements were exported to Excel (version 16.40). The distance between the two sides at anaphase onset was set to a maximum value (100%) and used to normalize the distance throughout ingression. In conditions where P₁ membranes visibly shift as a result of the AB cell division, the starting diameter of the P₁ cell was adjusted to the timepoint before any visible indentation of the membrane occurred. All *n* values were averaged for each timepoint, and plotted as a function of time in seconds. As the closure times were variable among cells, measurements were terminated when at least three cells had completed cytokinesis.

Measurements of the accumulation of actin, anillin and myosin at the midplane were performed on z-stack sum projections of a similar range of *z* in diploid and tetraploid embryos. A line was manually drawn along the cortex from the anterior to the posterior pole of the membrane at the furrow initiation phase, and both background and bleach corrections were made. To align the scans for each cell, a straight line was drawn in plane with the middle of the furrow region and used to determine the linescan value located in the center of the furrow region. Each linescan within a dataset was then aligned using this datapoint. Average values were calculated for each

location, and positions with fewer than 3 n were not included. X -axis values were multiplied by 0.16 to convert from pixels to microns, and the furrow position was set to 0. The area under the curve calculations were made in GraphPad Prism by setting the baseline to 50% of the peak value for each individual linescan, and including all intensities that fell within the baseline–peak range in the furrow region.

HILO images were falsely colored using the `mpl-inferno` LUT macro in FIJI to visualize differences in myosin intensity. Cool colors (violet, dark red) reflect weaker levels compared to brighter, warmer colors (orange, yellow). The ‘Zoom in Images and Stacks’ FIJI macro tool coded by Gilles Carpentier (Université Paris-Est Créteil Val de Marne, France; https://imagej.nih.gov/ij/macros/tools/Zoom_in_Images_and_Stacks.txt) was used to generate images with the zoom inset.

Quantitative data analysis

To measure the duration of the different phases of ring closure, graphs were analyzed using GraphPad Prism (version 8.4.3). A sigmoidal line of best fit was plotted using the averaged data for control AB and P_1 cells, then the second derivative of the best fit line with second order smoothing (four neighbors averaged) was plotted. The minimum and maximum x values (in seconds) of this second derivative curve represent the timepoints where there is a change of slope. The y value (% change in ring diameter) at the last timepoint of ring assembly, furrow initiation and ring constriction phases was noted for each control cell. These values were used as a cut-off to define phase transitions in individual cells of control and RNAi-treated embryos. Similarly, the second derivative of the sigmoidal line of best fit for averaged tetraploid AB and P_1 cell ingression curves was used to determine the phase transitions in tetraploid cell divisions. The phase duration for individual cells and their average was then plotted using GraphPad Prism.

To determine ring closure symmetry, 20 μm z -stacks of embryos expressing GFP::NMY-2 were imaged every 20 s. The position and size of the ring were manually extrapolated for each timepoint of division (from the start of the furrow initiation phase to maximum visible closure of the ring), temporally aligned, averaged and plotted. Briefly, straight lines were drawn in FIJI from one side of the ring to the other in each timepoint, and then rotated to align the long axis horizontally. A 250×50-pixel box was then drawn around this line. These regions were rotated in Python 3 (version 3.7.6) using SciKit Image (version 0.16.2) to produce an XZ view, and a projection was performed in FIJI to produce an image stack of the membrane. The ellipse tool was used to draw ellipses that matched the outline of the cell, and ellipse coordinates were recorded. In Python 3, a best-fit circle was plotted for each timepoint and each embryo. Coordinates were normalized to the first timepoint, where the center of the ring was at 0,0, and the radius at 1. The best-fit circle was averaged across all embryos within a group (n values are indicated in the figure panels) and plotted using the Jet colormap. To calculate symmetry, the Pythagorean formula was used to find the displacement of the middle of the ring at the last timepoint (last measurable opening of the ring) compared to the first timepoint (when there is any visible indentation of the membrane). Values greater than 0.2 were defined as asymmetric.

To determine the orientation of myosin filament bundles in a defined region of the furrow of dividing AB and P_1 cells, we used the Directionality plugin for FIJI. A region of the furrow was selected, and the plugin was run using the local gradient orientation method with 90 bins and a histogram from 0° to 90°. The plugin reports the frequency of filament bundles at a given angle, and fits a Gaussian function based on the highest peak in the histogram. The frequency values and Gaussian fit were plotted as a histogram in Excel. To have the center of the Gaussian fit be defined as straight (0°; perpendicular to the furrow region), we subtracted the peak Gaussian value from 0°. The proportion of filament bundles (sum of raw histogram values) that were within the center±two standard deviations of the Gaussian fit (referred to as the ‘Amount’) was considered to be well aligned. The change in the proportion of well-aligned filament bundles was calculated by subtracting the value from control.

All graphs except those for ring closure were plotted in GraphPad Prism and Excel. Ring closure symmetry graphs were plotted using Python 3 and Matplotlib (version 3.1.3). The full code for the ring closure and membrane

accumulation analyses is located at <http://github.com/cmci>. Graphs showing mean values are displayed with s.e.m. bars (indicated in the figure legends), and all n values are reported in the figure labels. All figures were prepared in Adobe Illustrator.

Pull-down assays and western blots

We purified recombinant ANI-1 protein to pull down importin- β from HeLa cell lysates. To do this we cloned the RBD+C2 from ANI-1 (708–1028) into pGEX4T and pMal vectors for protein expression. We also introduced the NLS mutations K938E and K940E or K947A and K949A into the pMal:ANI-1 vector by site-directed mutagenesis. The constructs and control empty vectors were transformed into *E. coli* BL21 cells, grown to an ideal OD and induced with IPTG as per the manufacturer’s instructions at 25°C (Sigma Aldrich for pGEX and New England Biolabs for pMal). Cells were resuspended in lysis buffer [2.5 mM MgCl_2 , 50 mM Tris-HCl, pH 7.5, 150 mM NaCl, 0.5% Triton X-100, 1 mM dithiothreitol (DTT), 1 mM phenylmethanesulfonyl fluoride (PMSF) and 1× protease inhibitors; Roche], then incubated with 1 mg/ml lysozyme on ice for 30 min and sonicated (1 min, 1 s on and 1 s off, 30% amplitude; Sonic Dismembrator Model 500, Fisher Scientific). After sonication and centrifugation, protein was purified by incubating with glutathione agarose (GST; Sigma Aldrich) or amylose resin (MBP; New England Biolabs) for 5 h at 4°C. The protein-bound beads were washed and stored as a 50% slurry at 4°C. Protein concentration was measured by running samples on SDS-PAGE stained with Coomassie Brilliant Blue and measured by densitometry against a standard curve of known BSA concentrations.

HeLa cells were cultured and transfected with a construct expressing Myc-tagged importin- β as previously described in Beaudet et al. (2017). Cells were washed then lysed on ice in lysis buffer (50 mM Tris-HCl, pH 7.6, 150 mM NaCl, 5 mM MgCl_2 , 0.5% Triton X-100, 1 mM DTT and 1 mM PMSF). To pull down Myc-importin- β , cell lysate was incubated at 4°C with 5–10 μg of purified GST or MBP-tagged ANI-1 protein bound to glutathione or amylose beads. The beads were washed several times with wash buffer (50 mM Tris-HCl, pH 7.6, 150 mM NaCl and 5 mM MgCl_2), after which sample buffer was added. Samples were run by SDS-PAGE, then wet-transferred to nitrocellulose for western blotting. Transfer efficiency was visualized by Ponceau S staining. Membranes were incubated with mouse anti-Myc antibodies (clone 9E10; Developmental Studies Hybridoma Bank; 1:250) for 2 h, and then washed and incubated with anti-mouse horseradish peroxidase (HRP)-conjugated secondary antibodies (Cedarlane Labs; 1:10,000) for 1–2 h. After washing, signal was detected using ECL western blotting detection reagents (GE Healthcare) and a GE Amersham Imager 6000, and the resulting images were converted to 8-bit using FIJI. Figures were prepared using Adobe Photoshop and Adobe Illustrator.

Statistical analysis

Statistical significance was determined using GraphPad Prism using unpaired Welch’s t -test with corrections for multiple comparisons made using the Holm–Šidák method (Figs 2F and 3C), or a two-way ANOVA with Šidák’s corrections for multiple comparisons (Figs 1C, 2C, 4C, 5C,H). Statistical significance was defined as: $P \geq 0.05$ not significant (ns); $*P \leq 0.05$, $**P \leq 0.01$, $***P \leq 0.001$, $****P \leq 0.0001$.

Acknowledgements

We thank the Piekny lab for discussions, Mathew Duguay for experimental support, Daniel Beaudet for experimental contributions and Mathieu C. Husser for help with analysis and editing. We thank J. C. Labbé (IRIC, Université de Montréal, Montréal, QC, Canada), A. S. Maddox (UNC Chapel Hill, NC, USA), S. W. Grill (Max Planck Institute of Molecular Cell Biology and Genetics, Dresden, Germany), and the *Caenorhabditis* Genetics Center (CGC) for worm strains. The CGC is funded by the Office of Research Infrastructure Programs, National Institutes of Health (P40 OD010440).

Competing interests

The authors declare no competing or financial interests.

Author contributions

Conceptualization: I.O., K.M., A.P.; Methodology: I.O., K.M., C.L.; Software: C.L.; Validation: I.O., K.M.; Formal analysis: I.O.; Investigation: I.O.; Writing - original draft: I.O., A.P.; Writing - review & editing: I.O., A.P.; Visualization: I.O.; Supervision: A.P.; Project administration: A.P.; Funding acquisition: A.P.

Funding

This work was funded by the Natural Sciences and Engineering Research Council of Canada (NSERC) [RGPIN-04161-2017 and CREATE-511601-2018].

Peer review history

The peer review history is available online at <https://journals.biologists.com/jcs/article-lookup/doi/10.1242/jcs.258921>.

References

- Amini, R., Goupil, E., Labella, S., Zetka, M., Maddox, A. S., Labbe, J.-C. and Chartier, N. T. (2014). C. elegans Anillin proteins regulate intercellular bridge stability and germline syncytial organization. *J. Cell Biol.* **206**, 129-143. doi:10.1083/jcb.201310117
- Askjaer, P., Galy, V., Hannak, E. and Mattaj, I. W. (2002). Ran GTPase cycle and importins α and β are essential for spindle formation and nuclear envelope assembly in living *Caenorhabditis elegans* embryos. *Mol. Biol. Cell* **13**, 4355-4370. doi:10.1091/mbc.e02-06-0346
- Bai, X., Melesse, M., Sorensen Turpin, C. G., Sloan, D. E., Chen, C.-Y., Wang, W.-C., Lee, P.-Y., Simmons, J. R., Nebenfuhr, B., Mitchell, D. et al. (2020). Aurora B functions at the apical surface after specialized cytokinesis during morphogenesis in *C. elegans*. *Development* **147**, dev181099. doi:10.1242/dev.181099
- Basant, A. and Glotzer, M. (2018). Spatiotemporal Regulation of RhoA during Cytokinesis. *Curr. Biol.* **28**, R570-R580. doi:10.1016/j.cub.2018.03.045
- Bauer, J., Poupart, V., Goupil, E., Nguyen, K. C. Q., Hall, D. H. and Labbe, J.-C. (2021). The initial expansion of the *C. elegans* syncytial germ line is coupled to incomplete primordial germ cell cytokinesis. *Development* **148**, dev199633. doi:10.1242/dev.199633
- Beaudet, D., Akhshi, T., Philipp, J., Law, C. and Piekny, A. (2017). Active Ran regulates anillin function during cytokinesis. *Mol. Biol. Cell* **28**, 3517-3531. doi:10.1091/mbc.e17-04-0253
- Beaudet, D., Pham, N., Skaik, N. and Piekny, A. (2020). Importin binding mediates the intramolecular regulation of anillin during cytokinesis. *Mol. Biol. Cell* **31**, 1124-1139. doi:10.1091/mbc.E20-01-0006
- Brenner, S. (1974). The genetics of *Caenorhabditis elegans*. *Genetics* **77**, 71-94. doi:10.1093/genetics/77.1.71
- Brownlee, C. and Heald, R. (2019). Importin α partitioning to the plasma membrane regulates intracellular scaling. *Cell* **176**, 805-815.e8. doi:10.1016/j.cell.2018.12.001
- Carvalho, A., Desai, A. and Oegema, K. (2009). Structural memory in the contractile ring makes the duration of cytokinesis independent of cell size. *Cell* **137**, 926-937. doi:10.1016/j.cell.2009.03.021
- Chan, C.-K. and Jans, D. A. (1999). Synergy of importin α recognition and DNA binding by the yeast transcriptional activator GAL4. *FEBS Lett.* **462**, 221-224. doi:10.1016/S0014-5793(99)01515-X
- Chan, F.-Y., Silva, A. M., Saramago, J., Pereira-Sousa, J., Brighton, H. E., Pereira, M., Oegema, K., Gassmann, R. and Carvalho, A. X. (2019). The ARP2/3 complex prevents excessive formin activity during cytokinesis. *Mol. Biol. Cell* **30**, 96-107. doi:10.1091/mbc.E18-07-0471
- Clarke, P. R. and Zhang, C. (2008). Spatial and temporal coordination of mitosis by Ran GTPase. *Nat. Rev. Mol. Cell Biol.* **9**, 464-477. doi:10.1038/nrm2410
- Clarke, E. K., Gomez, K. A. R., Mustachi, Z., Murph, M. C. and Schwarzstein, M. (2018). Manipulation of Ploidy in *Caenorhabditis elegans*. *J. Vis. Exp.* (133), e57296. doi:10.3791/57296
- Cowan, C. R. and Hyman, A. A. (2007). Acto-myosin reorganization and PAR polarity in *C. elegans*. *Development* **134**, 1035-1043. doi:10.1242/dev.000513
- Davies, T., Kim, H. X., Romano Spica, N., Lesea-Pringle, B. J., Dumont, J., Shirasu-Hiza, M. and Canman, J. C. (2018). Cell-intrinsic and -extrinsic mechanisms promote cell-type-specific cytokinetic diversity. *eLife* **7**, e36204. doi:10.7554/eLife.36204
- Dechant, R. and Glotzer, M. (2003). Centrosome separation and central spindle assembly act in redundant pathways that regulate microtubule density and trigger cleavage furrow formation. *Dev. Cell* **4**, 333-344. doi:10.1016/S1534-5807(03)00057-1
- Deng, M., Suraneni, P., Schultz, R. M. and Li, R. (2007). The Ran GTPase mediates chromatin signaling to control cortical polarity during polar body extrusion in mouse oocytes. *Dev. Cell* **12**, 301-308. doi:10.1016/j.devcel.2006.11.008
- Evans, T. C. (2006). Transformation and microinjection. In *WormBook* (ed. The *C. elegans* Research Community). Wormbook. doi:10.1895/wormbook.1.108.1
- Gan, W. J. and Motegi, F. (2020). Mechanochemical control of symmetry breaking in the *Caenorhabditis elegans* Zygote. *Front. Cell Dev. Biol.* **8**, 619869. doi:10.3389/fcell.2020.619869
- Geles, K. G. and Adam, S. A. (2001). Germline and developmental roles of the nuclear transport factor importin α 3 in *C. elegans*. *Development* **128**, 1817-1830. doi:10.1242/dev.128.10.1817
- Giesecke, A. and Stewart, M. (2010). Novel Binding of the mitotic regulator TPX2 (target protein for *Xenopus* kinesin-like protein 2) to importin- α . *J. Biol. Chem.* **285**, 17628-17635. doi:10.1074/jbc.M110.102343
- Goupil, E., Amini, R., Hall, D. H. and Labbe, J.-C. (2017). Actomyosin contractility regulators stabilize the cytoplasmic bridge between the two primordial germ cells during *Caenorhabditis elegans* embryogenesis. *Mol. Biol. Cell* **28**, 3789-3800. doi:10.1091/mbc.e17-08-0502
- Green, R. A., Paluch, E. and Oegema, K. (2012). Cytokinesis in animal cells. *Annu. Rev. Cell Dev. Biol.* **28**, 29-58. doi:10.1146/annurev-cellbio-101011-155718
- Gruss, O. J., Carazo-Salas, R. E., Schatz, C. A., Guarguaglini, G., Kast, J., Wilm, M., Le Bot, N., Vernos, I., Karsenti, E. and Mattaj, I. W. (2001). Ran induces spindle assembly by reversing the inhibitory effect of importin α on TPX2 activity. *Cell* **104**, 83-93. doi:10.1016/S0092-8674(01)00193-3
- Hasegawa, K., Ryu, S. J. and Kalab, P. (2013). Chromosomal gain promotes formation of a steep RanGTP gradient that drives mitosis in aneuploid cells. *J. Cell Biol.* **200**, 151-161. doi:10.1083/jcb.201206142
- Hickson, G. R. X. and O'farrell, P. H. (2008). Rho-dependent control of anillin behavior during cytokinesis. *J. Cell Biol.* **180**, 285-294. doi:10.1083/jcb.200709005
- Hoeg, C. and Hyman, A. A. (2013). Principles of PAR polarity in *Caenorhabditis elegans* embryos. *Nat. Rev. Mol. Cell Biol.* **14**, 315-322. doi:10.1038/nrm3558
- Husser, M. C., Skaik, N., Martin, V. J. J. and Piekny, A. (2021). CRISPR-Cas tools to study gene function in cytokinesis. *J. Cell Sci.* **134**, jcs254409.
- Illukkumbura, R., Bland, T. and Goehring, N. W. (2020). Patterning and polarization of cells by intracellular flows. *Curr. Opin. Cell Biol.* **62**, 123-134. doi:10.1016/j.cob.2019.10.005
- Kalab, P., Weis, K. and Heald, R. (2002). Visualization of a Ran-GTP gradient in interphase and mitotic *Xenopus* egg extracts. *Science* **295**, 2452-2456. doi:10.1126/science.1068798
- Kalab, P., Pralle, A., Isacoff, E. Y., Heald, R. and Weis, K. (2006). Analysis of a RanGTP-regulated gradient in mitotic somatic cells. *Nature* **440**, 697-701. doi:10.1038/nature04589
- Kamath, R. S., Martinez-Campos, M., Zipperlen, P., Fraser, A. G. and Ahringer, J. (2001). Effectiveness of specific RNA-mediated interference through ingested double-stranded RNA in *Caenorhabditis elegans*. *Genome Biol.* **2**, 1-10.
- Kemphues, K. J., Priess, J. R., Morton, D. G. and Cheng, N. S. (1988). Identification of genes required for cytoplasmic localization in early *C. elegans* embryos. *Cell* **52**, 311-320. doi:10.1016/S0092-8674(88)80024-2
- Khalilullin, R. N., Green, R. A., Shi, L. Z., Gomez-Cavazos, J. S., Berns, M. W., Desai, A. and Oegema, K. (2018). A positive-feedback-based mechanism for constriction rate acceleration during cytokinesis in *Caenorhabditis elegans*. *eLife* **7**, e36073. doi:10.7554/eLife.36073
- Kiyomitsu, T. and Cheeseman, I. M. (2013). Cortical dynein and asymmetric membrane elongation coordinately position the spindle in anaphase. *Cell* **154**, 391-402. doi:10.1016/j.cell.2013.06.010
- Lewellyn, L., Dumont, J., Desai, A. and Oegema, K. (2010). Analyzing the effects of delaying aster separation on furrow formation during cytokinesis in the *Caenorhabditis elegans* embryo. *Mol. Biol. Cell* **21**, 50-62. doi:10.1091/mbc.e09-01-0089
- Maddox, A. S., Lewellyn, L., Desai, A. and Oegema, K. (2007). Anillin and the septins promote asymmetric ingression of the cytokinetic furrow. *Dev. Cell* **12**, 827-835. doi:10.1016/j.devcel.2007.02.018
- Mangal, S., Sacher, J., Kim, T., Osório, D. S., Motegi, F., Carvalho, A. X., Oegema, K. and Zanin, E. (2018). TPXL-1 activates Aurora A to clear contractile ring components from the polar cortex during cytokinesis. *J. Cell Biol.* **217**, 837-848. doi:10.1083/jcb.201706021
- Mishima, M., Kaitna, S. and Glotzer, M. (2002). Central spindle assembly and cytokinesis require a kinesin-like protein/RhoGAP complex with microtubule bundling activity. *Dev. Cell* **2**, 41-54. doi:10.1016/S1534-5807(01)00110-1
- Munro, E., Nance, J. and Priess, J. R. (2004). Cortical flows powered by asymmetrical contraction transport PAR proteins to establish and maintain anterior-posterior polarity in the early *C. elegans* embryo. *Dev. Cell* **7**, 413-424. doi:10.1016/j.devcel.2004.08.001
- Nachury, M. V., Maresca, T. J., Salmon, W. C., Waterman-Storer, C. M., Heald, R. and Weis, K. (2001). Importin β is a mitotic target of the small GTPase Ran in spindle assembly. *Cell* **104**, 95-106. doi:10.1016/S0092-8674(01)00194-5
- Osorio, D. S., Chan, F.-Y., Saramago, J., Leite, J., Silva, A. M., Sobral, A. F., Gassmann, R. and Carvalho, A. X. (2019). Crosslinking activity of non-muscle myosin II is not sufficient for embryonic cytokinesis in *C. elegans*. *Development* **146**, dev179150. doi:10.1242/dev.179150
- Ozugerlin, I. and Piekny, A. (2021). Complementary functions for the Ran gradient during division. *Small GTPases* **12**, 177-187. doi:10.1080/21541248.2020.1725371

- Piekny, A. J. and Glotzer, M.** (2008). Anillin is a scaffold protein that links Rhoa, actin, and myosin during cytokinesis. *Curr. Biol.* **18**, 30–36. doi:10.1016/j.cub.2007.11.068
- Piekny, A. J. and Maddox, A. S.** (2010). The myriad roles of Anillin during cytokinesis. *Semin. Cell Dev. Biol.* **21**, 881–891. doi:10.1016/j.semcdb.2010.08.002
- Piekny, A., Werner, M. and Glotzer, M.** (2005). Cytokinesis: welcome to the Rho zone. *Trends Cell Biol.* **15**, 651–658. doi:10.1016/j.tcb.2005.10.006
- Pimpale, L. G., Middelkoop, T. C., Mietke, A. and Grill, S. W.** (2020). Cell lineage-dependent chiral actomyosin flows drive cellular rearrangements in early *Caenorhabditis elegans* development. *eLife* **9**, e54930. doi:10.7554/eLife.54930
- Price, K. L. and Rose, L. S.** (2017). LET-99 functions in the astral furrowing pathway, where it is required for myosin enrichment in the contractile ring. *Mol. Biol. Cell* **28**, 2360–2373. doi:10.1091/mbc.e16-12-0874
- Reymann, A.-C., Staniscia, F., Erzberger, A., Salbreux, G. and Grill, S. W.** (2016). Cortical flow aligns actin filaments to form a furrow. *eLife* **5**, e17807. doi:10.7554/eLife.17807
- Rodrigues, N. T. L., Lekontsev, S., Jananji, S., Kriston-Vizi, J., Hickson, G. R. X. and Baum, B.** (2015). Kinetochore-localized PP1-Sds22 couples chromosome segregation to polar relaxation. *Nature* **524**, 489–492. doi:10.1038/nature14496
- Rose, L. and Gonczy, P.** (2014). Polarity establishment, asymmetric division and segregation of fate determinants in early *C. elegans* embryos. In *WormBook* (ed. The *C. elegans* Research Community). Wormbook. doi: 10.1895/wormbook.1.30.2
- Schatz, C. A., Santarella, R., Hoenger, A., Karsenti, E., Mattaj, I. W., Gruss, O. J. and Carazo-Salas, R. E.** (2003). Importin α -regulated nucleation of microtubules by TPX2. *EMBO J.* **22**, 2060–2070. doi:10.1093/emboj/cdg195
- Silljé, H. H. W., Nagel, S., Körner, R. and Nigg, E. A.** (2006). HURP Is a Ran-importin β -regulated protein that stabilizes kinetochore microtubules in the vicinity of chromosomes. *Curr. Biol.* **16**, 731–742. doi:10.1016/j.cub.2006.02.070
- Silva, A. M., Osório, D. S., Pereira, A. J., Maiato, H., Pinto, I. M., Rubinstein, B., Gassmann, R., Telley, I. A. and Carvalho, A. X.** (2016). Robust gap repair in the contractile ring ensures timely completion of cytokinesis. *J. Cell Biol.* **215**, 789–799. doi:10.1083/jcb.201605080
- Singh, D. and Pohl, C.** (2014). Coupling of rotational cortical flow, asymmetric midbody positioning, and spindle rotation mediates dorsoventral axis formation in *C. elegans*. *Dev. Cell* **28**, 253–267. doi:10.1016/j.devcel.2014.01.002
- Somers, W. G. and Saint, R.** (2003). A RhoGEF and Rho family GTPase-activating protein complex links the contractile ring to cortical microtubules at the onset of cytokinesis. *Dev. Cell* **4**, 29–39. doi:10.1016/S1534-5807(02)00402-1
- Strome, S. and Wood, W. B.** (1982). Immunofluorescence visualization of germ-line-specific cytoplasmic granules in embryos, larvae, and adults of *Caenorhabditis elegans*. *Proc. Natl. Acad. Sci. USA* **79**, 1558–1562. doi:10.1073/pnas.79.5.1558
- Tokunaga, M., Imamoto, N. and Sakata-Sogawa, K.** (2008). Highly inclined thin illumination enables clear single-molecule imaging in cells. *Nat. Methods* **5**, 159–161. doi:10.1038/nmeth1171
- Tse, Y. C., Piekny, A. and Glotzer, M.** (2011). Anillin promotes astral microtubule-directed cortical myosin polarization. *Mol. Biol. Cell* **22**, 3165–3175. doi:10.1091/mbc.e11-05-0399
- Tse, Y. C., Werner, M., Longhini, K. M., Labbe, J.-C., Goldstein, B. and Glotzer, M.** (2012). RhoA activation during polarization and cytokinesis of the early *Caenorhabditis elegans* embryo is differentially dependent on NOP-1 and CYK-4. *Mol. Biol. Cell* **23**, 4020–4031. doi:10.1091/mbc.e12-04-0268
- van Oostende Triplet, C., Jaramillo Garcia, M., Haji Bik, H., Beaudet, D. and Piekny, A.** (2014). Anillin interacts with microtubules and is part of the astral pathway that defines cortical domains. *J. Cell Sci.* **127**, 3699–3710. doi:10.1242/jcs.147504
- Wiese, C., Wilde, A., Moore, M. S., Adam, S. A., Merdes, A. and Zheng, Y.** (2001). Role of importin- β in coupling Ran to downstream targets in microtubule assembly. *Science* **291**, 653–656. doi:10.1126/science.1057661
- Xu, L. and Massague, J.** (2004). Nucleocytoplasmic shuttling of signal transducers. *Nat. Rev. Mol. Cell Biol.* **5**, 209–219. doi:10.1038/nrm1331
- Yuce, O., Piekny, A. and Glotzer, M.** (2005). An ECT2-centralspindlin complex regulates the localization and function of RhoA. *J. Cell Biol.* **170**, 571–582. doi:10.1083/jcb.200501097
- Zanin, E., Desai, A., Poser, I., Toyoda, Y., Andree, C., Moebius, C., Bickle, M., Conradt, B., Piekny, A. and Oegema, K.** (2013). A conserved RhoGAP limits M phase contractility and coordinates with microtubule asters to confine RhoA during cytokinesis. *Dev. Cell* **26**, 496–510. doi:10.1016/j.devcel.2013.08.005